Numerical modelling of traditional buildings composed of timber frames and masonry walls under seismic loading

Belén Jiménez[a,b]* and Luca Pelà[a]

[a]Department of Civil and Environmental Engineering
Universitat Politécnica de Catalunya (UPC-BarcelonaTech)
Jordi Girona 1-3, 08034 Barcelona, Spain

[b]Department of Architecture
Universidad Técnica Federico Santa María
Vicuña Mackenna 3939, San Joaquín, Región Metropolitana, Chile

*e-mail: belen.jimenez@usm.cl , luca.pela@upc.edu

Abstract – Existing heritage buildings are often composed of diverse materials and structural typologies, representing a challenge for structural analysis tasks. This work investigates the combined use of simple Lumped Plasticity Models (LPM) and macro-mechanical Finite Element (FE) approaches to evaluate the seismic response of structures composed of timber frames and masonry walls. The calibration of these engineering models is derived from a wide set of nonlinear static analyses reproducing benchmark experiments on timber and masonry specimens. The LPM and FE models are used eventually to appraise the seismic response of two existing timber-masonry hybrid buildings, located in the historical centre of Valparaíso, Chile. The nonlinear analyses performed with these models predict the acceleration-displacement capacity of the buildings under seismic-like horizontal loading, revealing their potential local and global failure mechanisms.

Keywords: Nonlinear Static Analysis, Timber Frame, Unreinforced Masonry Walls, Numerical Simulation, Lumped Plasticity Models, Macro-Mechanical FE Models

1. Introduction

Timber and masonry are recurrent materials in traditional and historical construction. A large part of the built heritage is composed of timber and masonry structural typologies, and the need for their conservation requires reliable tools and methods for their analysis and assessment. The

evaluation of the structural safety of these types of buildings against natural hazards, such as earthquakes, is a central issue in nowadays research.

The most of the available structural modelling strategies deal with timber or masonry structures separately, i.e. considering homogeneous structural systems built with a single material (Lukic et al. 2018; González and Gutiérrez 2005; Vieux-champagne et al. 2014; Kouris et al. 2014; S. Saloustros, Pelà, and Roca 2020; D'Ambra, Lignola, and Prota 2016; Kalkbrenner, Pelà, and Sandoval 2019). Few researchers have addressed the modelling of hybrid timber-masonry structures (Ciocci, Sharma, and Lourenço 2018; Kouris and Kappos 2014; Quinn 2016; Perrone 2011). The lack of experimental data about hybrid typologies, where timber frames coexist with load-bearing masonry walls, constitutes a major drawback in the calibration process of numerical models for the structural analysis of existing buildings.

The modelling of timber frames can be addressed by using simplified Lumped Plasticity Models (LPM), where linear elastic frame elements are used to represent the timber members, while nonlinear springs or hinges introduce the nonlinearities at the nodes of the frames. LPM constitutes a suitable approach to simulate the structural behaviour of timber frame structures, after assuming that plasticisation occurs at the connections, i.e. the frame members' ends. In these cases, experimental or analytical approaches are fundamental to evaluate the nonlinear behaviour of the connections. The definition of proper nonlinear moment-rotation or force-displacement relationships for the rotational hinges or axial springs at the connections is a central step to ensure reliable numerical simulations. The advantages of LPM lie in the simplicity of the parameters' definition, as well as in the low computational costs, which allow practice-oriented simulations applicable to entire buildings or large-scale applications. However, the reliable calibration of the lumped nonlinearities is a key issue during the preparation of the numerical model.

The numerical simulation of unreinforced masonry structures (URM) has experienced a remarkable development in the last decades. The diversity of modelling needs has driven to the

development of several approaches with different levels of detail regarding the material discretization (Roca et al. 2010). Finite Elements (FE) continuum macro-mechanical modelling approaches are commonly adopted to address simplified and practice-oriented simulations of masonry walls subjected to in-plane and out-of-plane actions (Saloustros et al. 2017b; Saloustros, Cervera, and Pelà 2019; Pantò et al. 2019; Kouris and Kappos 2012; D'Ambra, Lignola, and Prota 2016; Endo et al. 2015; Bilgin and Korini 2014; Spyrakos and Francioso 2012). Macro-models do not make any distinction between units and mortar joints, and masonry is represented as a continuous homogeneous material in a simplified manner. The material behaviour is represented by using proper constitutive laws simulating the nonlinear response of masonry under different types of loads.

This paper presents a methodology to build simplified and practice-oriented numerical models for the analysis of hybrid timber-masonry buildings. The study covers the definition of proper LPM for timber frames, and the formulation of a FE continuum macro-mechanical model for masonry walls. The central issue of the calibration of the models is pursued by means of a rigorous and scientific approach, based on the careful comparison between a wide set of available experiments on timber frames and masonry walls, and the results from the numerical simulations of the tests. The procedure includes the analysis of five benchmark experiments on timber frames, both bare and infilled, and three experiments on masonry walls, both in-plane and out-of-plane loaded. The calibrated models are used to simulate the seismic behaviour of two real traditional timber-masonry buildings located in the city of Valparaíso (Chile). All the models were developed within the structural and earthquake engineering software SAP2000 (v20).

2. Calibration of the numerical model

2.1 Numerical simulation of experiments on bare timber frames

This section presents the calibration of the timber frame models by simulating the experimental behaviour of traditional Pombalino and *Quincha* walls. The adoption of Pombalino

frames became common in Portugal after the devastating Lisbon Earthquake. These buildings were intended to be anti-seismic, being characterized by a "cage" braced structure with St. Andrew's crosses (Poletti 2013). Similarly, the *quincha* walls were introduced in Lima (Peru) after strong earthquakes destroyed the adobe houses during the sixteenth and seventeenth centuries. The second floors of the houses were rebuilt with *quincha* walls, which demonstrated a good seismic behaviour in later earthquakes. *Quicha* walls are still used in Peru but also in other countries of Latin America (Torrealva, Vicente, and Michiels 2018).

The calibration of the LPM for timber frames was developed by simulating five benchmark experimental tests on both bare and infilled frames of Portuguese Pombalino and Peruvian *quincha* walls, all tested under vertical pre-compression and lateral loads (Figure 1). Nonlinear static analysis (NSA) under displacement control was executed to obtain the structural behaviour of the models.

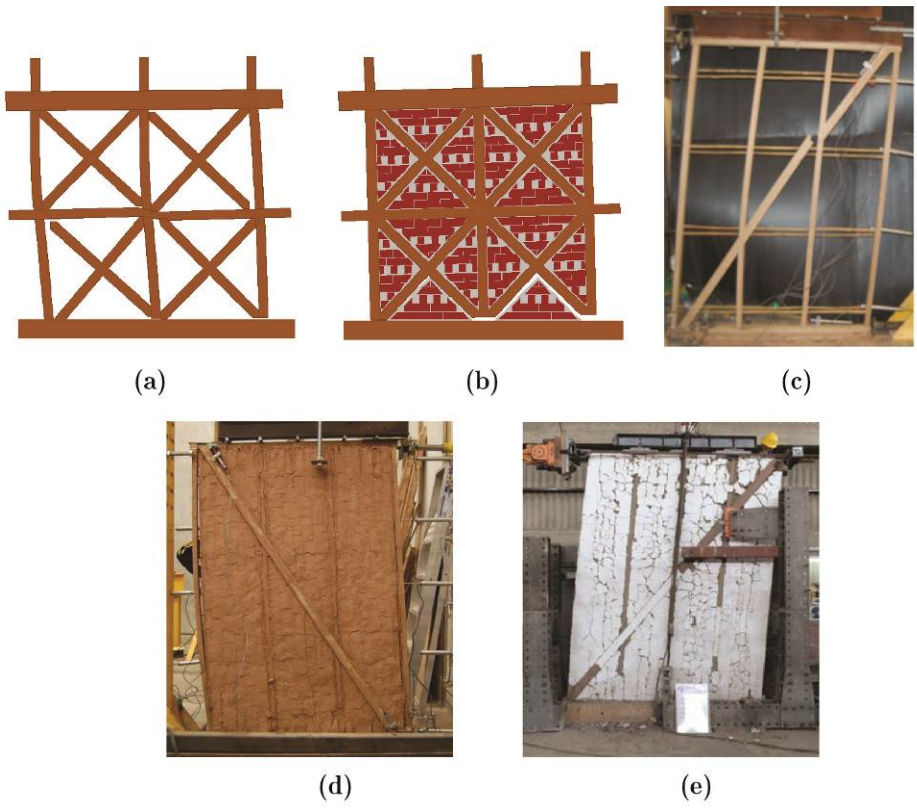

Figure 1. Benchmark experimental tests on timber frame walls: (a-b) bare and infilled Pombalino frames (Poletti and Vasconcelos 2015), (c-d) bare and infilled Quincha frames tested in half-scale (Moore and D'Ayala 2011), and (e) infilled Quincha frames tested in full-scale (Torrealva, Vicente, and Michiels 2018).

An experimental campaign on the Pombalino timber frame typology carried out by Poletti

(2013) was first selected to validate the numerical modelling strategy. Both a bare frame and an infilled specimen, subjected to the same loading conditions, were selected for simulation to study the influence of the infill on the lateral response (Figure 1a-b).

The LPM was composed of top and bottom beams of 0.16 × 0.12 m^2 cross-section, while the post and diagonal elements had a 0.08 × 0.12 m^2 cross-section, as shown in Figure 2a. The connections between beams and posts, as well as those among intersecting diagonals, were made of half-lap carpentry joints, while the connections between the main frame and the diagonals were made by contact, as shown in Figure 2c. The timber was modelled as a linear elastic isotropic homogeneous material, considering the mechanical properties reported in Poletti (2013). A vertical load of 25 kN was applied at each post to represent realistically the loading condition encountered on site, as reported in Poletti &Vasconcelos (2015). A lateral displacement of 0.1 m was applied at the top-left corner as in the experiment. The LPM frame was pinned-supported at the base and restrained in the horizontal direction at the top-left node to allow the displacement application, in agreement with the experimental boundary conditions.

Modelling and calibration of the behaviour of the carpentry joint connections was a fundamental stage during the preparation of the LPM models. Nonlinear rotational hinges were introduced into the model in the locations of the half-lap connections, as shown in Figure 2b. A specific laboratory test on a half-lap connection specimen (Poletti 2013) allowed the determination of the nonlinear rotational behaviour, expressed in terms of a moment-rotation relationship with stiffness values K_{in} = 171 kNm/rad and K_{fin} = 47 kNm/rad, see Figure 2c (Poletti, Lourenco, and Ciocci 2016).

Sensitivity analyses were performed to calibrate the nonlinear behaviour of the connections by contact according to Ciocci (2015), due to the lack of specific experimental data. Linear spring elements were introduced at the end nodes of diagonal members, together with moment releases (Figure 2b). These elements were aligned with the longitudinal and transverse local axes of the

diagonal member. Their axial and shear stiffnesses were modified progressively until the value of 9050 kN/m, in order to reproduce a good agreement between the initial stiffness of the model and the experimental one. Figure 2d-f show the axial and shear nonlinear laws of the connection by contact. The axial and shear stiffnesses were assumed equal for the sake of simplicity, due to the lack of specific experimental datasets about the behaviour of connection by contacts in the available scientific literature. Since the compressive strength was not derived from the experimental tests, different values of the yielding load F_y were considered until obtaining a good agreement between the model and the experimental results for F_y = 26 kN. According to Ciocci (2015), the ultimate displacement of the connection by contact can be assumed as the same one reached by the half-lap connection (d_u = 0.05 m) since after the central connection failed, the remaining connections no longer worked. The ultimate capacity of the connections by contact was assumed zero when the ultimate displacement d_u was reached.

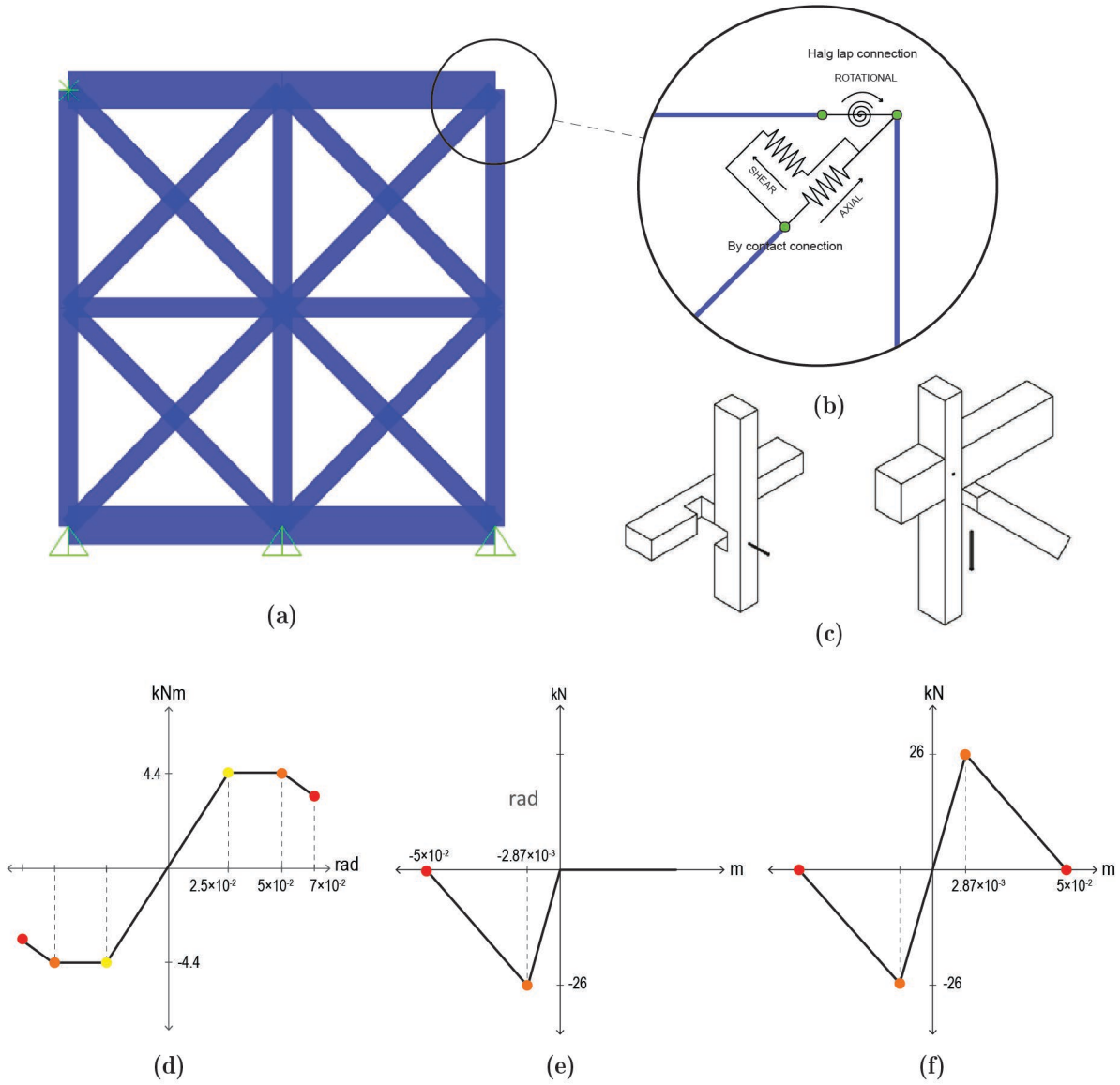

Figure 2. LPM of the Pombalino bare frame: (a) view of the FE model, (b) zoom of spring elements in a joint, (c) sketches of half-lap and connections by contact, (d) half-lap joint rotational behaviour, (e) axial and (f) shear responses of connection by contact.

Figure 3a shows the load-displacement capacity curves of the model for varying values of F_y. The collapse mechanism predicted by the model revealed a very good agreement with the observed experimental response of the bare frame. Figure 3a highlights also the instances A-E corresponding to the nonlinearities appeared during the simulations. Figure 3b shows the evolution of the so-called "plastic state" of the hinges within the model during the development of the analysis, with dots of different colours according to the reached magnitude of plastic displacement/rotation (see Figure 2b). Nonlinearities started to appear at 0.017 m global displacement, when the axial springs of the

compressed diagonals reached their maximum capacity. Subsequently, the rotational hinges located at the central and external post-beam connections plasticized, and the model failed when the central ones reached their ultimate capacity. As in the experiment, the shear effect provoked by the diagonal on the central node led to the failure of this connection. Once this happened, the diagonals no longer worked and the analysis stopped at a displacement of 0.088 m.

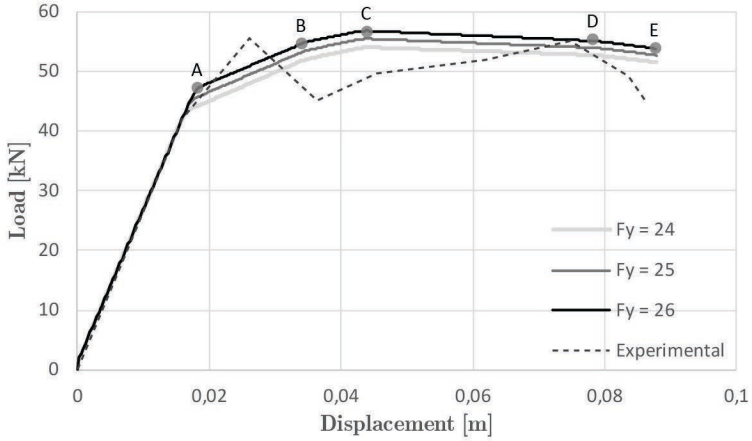

(a)

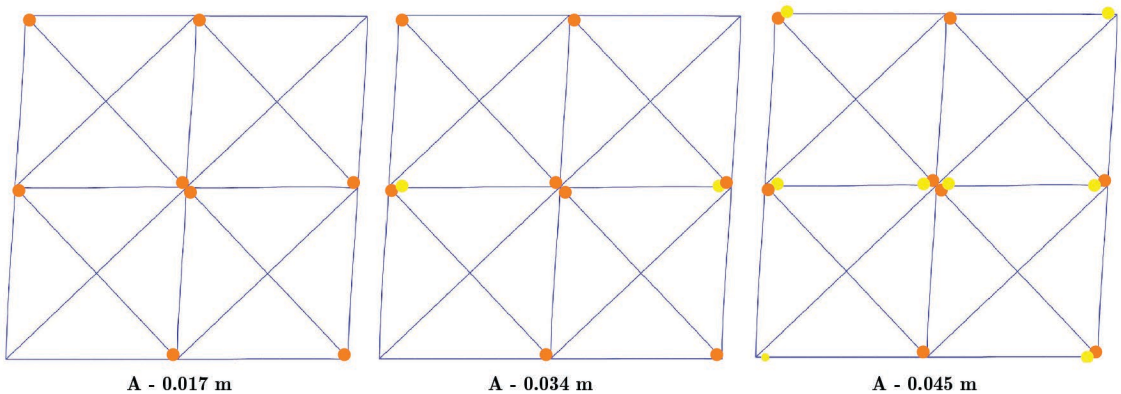

A - 0.017 m A - 0.034 m A - 0.045 m

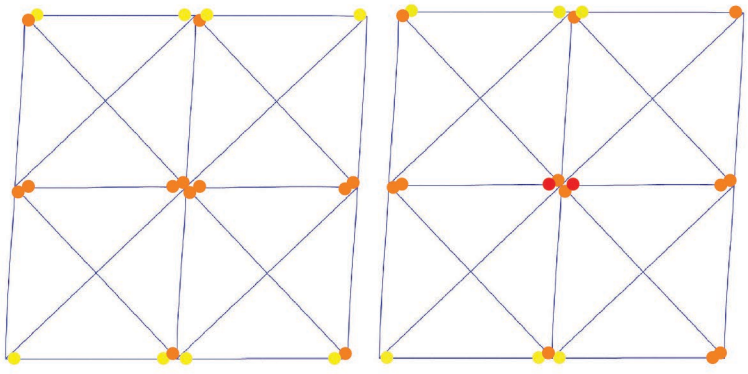

D - 0.08 m E - 0.088 m

(b)

Figure 3. LPM of the Pombalino bare frame: a) load vs. displacement curves derived from parametric analysis of the capacity of the connection by contact, b) evolution of the collapse mechanism, according to the plastic states denoted in Figure 2b.

The second benchmark experiment was the *quincha* frame tested in half-scale dimension by Moore and D'Ayala (2011), see Figure 1c. The LPM was composed of post and beam elements with 0.06×0.08 m^2 cross-section, while the diagonal had 0.09×0.03 m^2 cross-section, as shown in Figure 4a. The timber specimens were modelled using the elastic isotropic material properties reported in Quinn (2015). Mortise-and-tenon joints were used to connect the posts and beams, while the diagonal was fastened to the frame using nails, see Figure 4b. A pre-compression load of 4.4 kN/m was applied through the top beam, followed by an incremental horizontal displacement applied at the top-left node to simulate the loading conditions during the experiment. The nodes at the base were restrained in all the translational DOFs. Nonlinear axial springs were introduced at each node of the diagonal-frame connections. Moment releases were specified at each end node of the diagonal to avoid the moment resistance at these points.

The experimental moment-rotation response obtained in the same campaign was used to define the nonlinear relationship of this type of the mortise-and-tenon connection in the model, see Figure 4c. Nonlinear rotational hinges were used to introduce the nonlinearities at the top post-beam nodes of the model (see Figure 2b). According to Quinn (2016), the uplift experienced by the mortise-and-tenon joints at the bottom of the frame could be represented by defining the tensile elastic capacity of these connections, based on the vertical uplift measurements on the tested frame. This relationship was used to model the axial stiffness of the springs attached at the bottom post-beam connections of the model.

Analytical calculations were developed in order to predict the nonlinear behaviour of the nailed connection at the ends of the diagonal member since no experimental data were available. The capacity of the nails was calculated by using the equations proposed by Eurocode 5 (CEN EC5 1.2 2004) for laterally loaded nails in single shear. This approach considers most of the essential parameters governing the response of nailed connections such as the mechanical properties of the

materials, the grain direction, the geometry and number of the nails, and the type of loads. Further details about calculations are reported in Jiménez (2021).

The capacity of the nailed connections was assessed by means of a sensitivity analysis with different yielding tensile strength (f_y) of the nails in the model, as no experimental data were available. Different reasonable yielding tensile strength values of commercial nails were considered to perform the sensitivity analysis, with f_y equal to 500, 600 and 690 N/mm^2, according to Porteous and Kermani (2004), corresponding to yielding loads F_y of 1.54 kN, 1.68 kN and 1.80 kN, respectively. The load-deformation relationship of the nailed connections was defined assuming a bilinear curve with an initial linear branch up to the maximum capacity of the connection, followed by a softening behaviour. The stiffness and yield displacement of the connection were determined through a sensitivity analysis until obtaining a good agreement between the model and the experiment. The response of the model was in good agreement with the experiment, assuming a linear stiffness of 2130 kN/m and a maximum capacity of 1.80 N/mm^2 for the nailed connections. The yield displacement d_y of the connection was calculated as 8.45×10^{-4} m, while its ultimate displacement was 5×10^{-3} m by applying a sensitivity analysis.

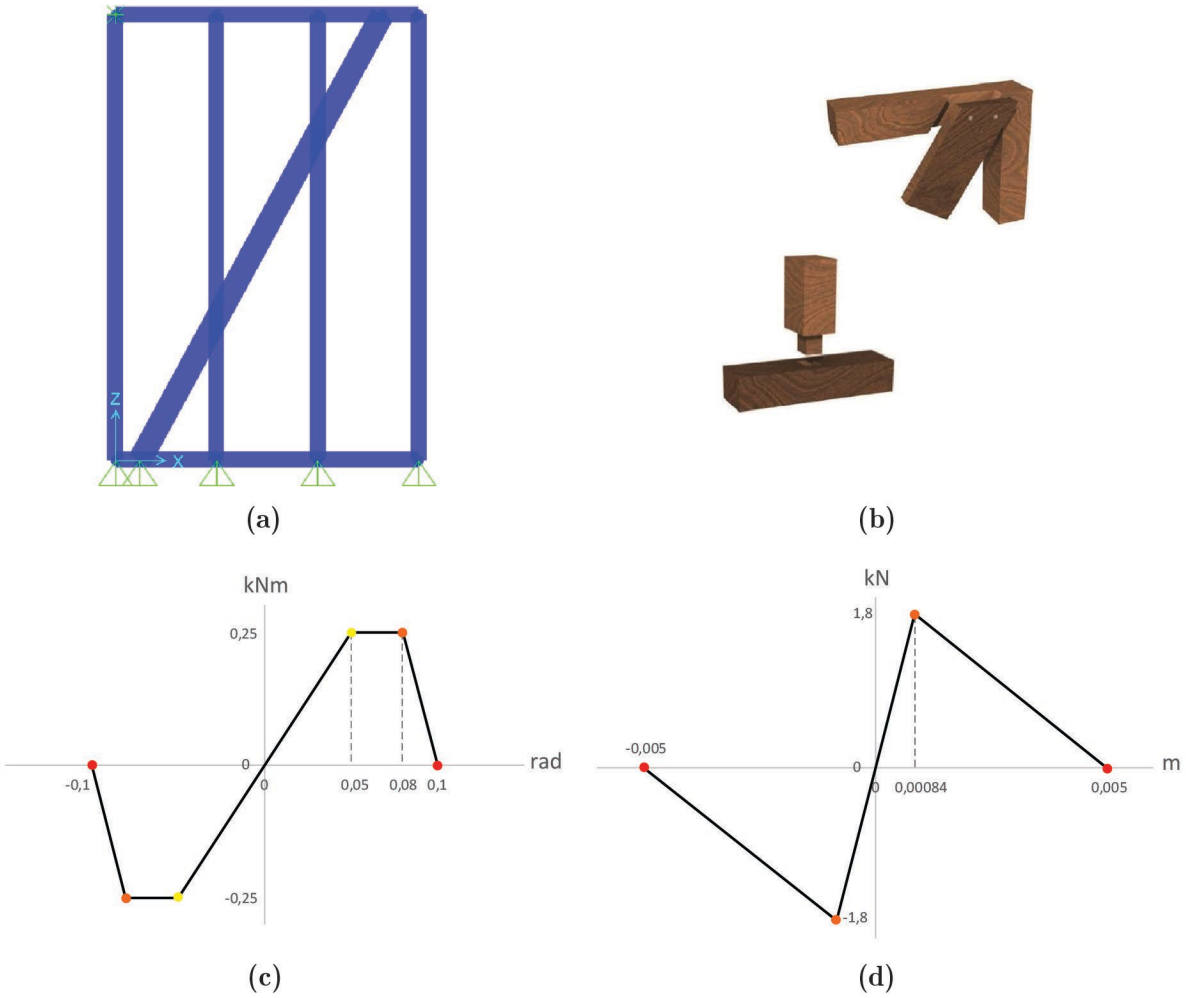

Figure 4. LPM of the half-scale Quincha bare frame: (a) view of the FE model, (b) sketches of mortise-and-tenon joints and nailed connections, (c) mortise-and-tenon rotational behaviour, and (d) nailed connection shear behaviour.

The collapse mechanism predicted by the model was in good agreement with that observed during the experiment. Figure 5b displays the instances A-D of local failures during the simulation, while Figure 5c shows the evolution of the so-called "plastic state" of the hinges and springs within the model during the development of the analysis, according to Figure 4c-d. Nonlinearities appeared at the bottom diagonal connection when the spring reached its maximum capacity at a displacement of 0.01 m. After this point, the remaining springs along the diagonal and some of the top hinges reached their maximum capacity. As in the experiment, the frame failed as soon as the top diagonal-beam connection reached its ultimate capacity.

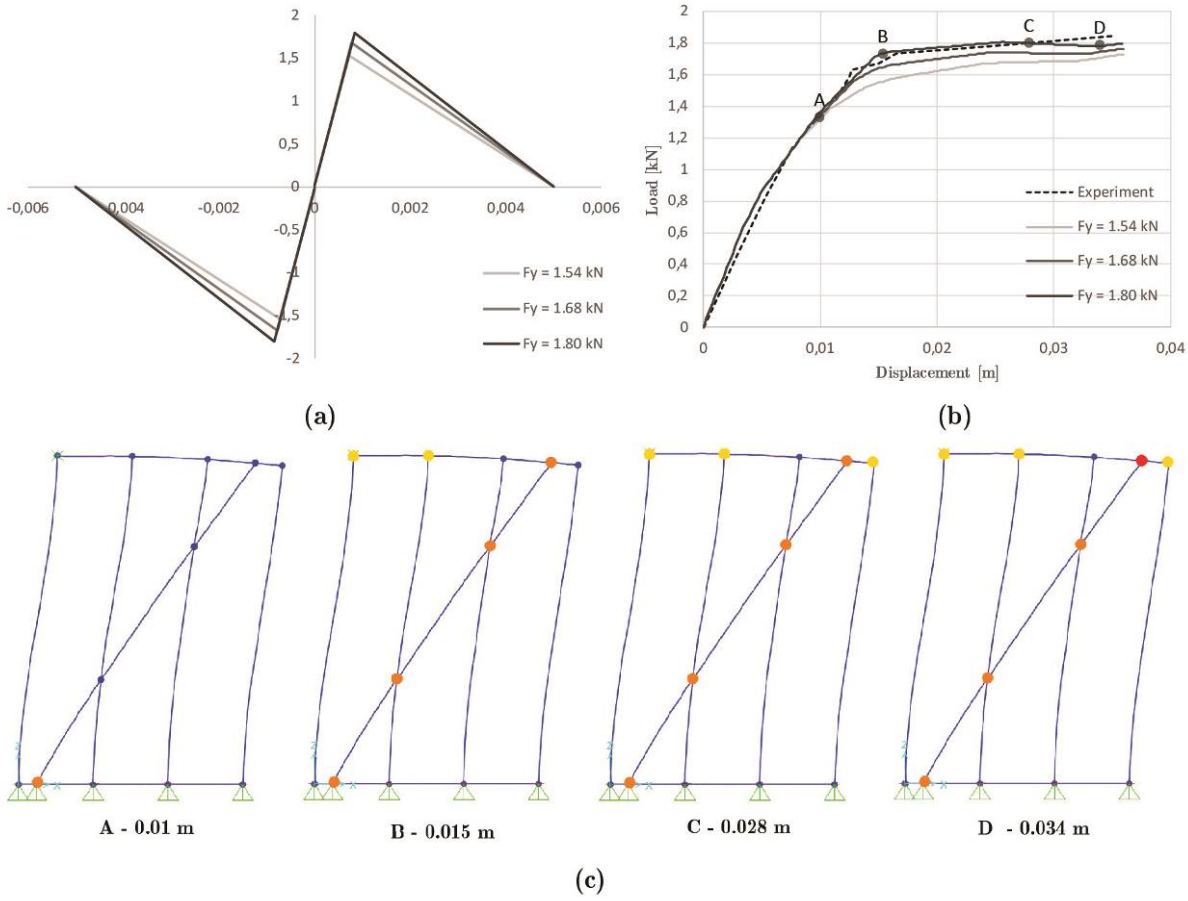

Figure 5. LPM of the half-scale Quincha bare frame: (a-b) load vs. displacement curves derived from parametric analysis of the capacity of the nailed connections, and (c) evolution of the collapse mechanism, according to the plastic states denoted in Figure 4b.

2.2 Numerical simulation of experiments on infilled timber frames

The modelling of the infill was addressed using the Equivalent Strut Method (ESM), originally introduced by Stafford-Smith (1963) and subsequently developed by Bertoldi, Decanini, and Gavarini (1993). This study allowed estimating the contribution of the infill within the bare frame models. The ESM is a simplified approach where the elastic in-plane stiffness of an uncracked solid masonry infill is represented with an equivalent strut (Figure 6a), whose width ω is given by Equation (1). Such a strut shall have the same thickness and modulus of elasticity of the infill panel that it represents. According to Stafford-Smith (1963), the equivalent width of the strut depends on a relative stiffness parameter λ_h given by Equation (2), and on the constants k_1 and k_2 also related to λ_h. The

choice of what values to assign to these constants varies in the available scientific literature, based on different experimental studies. The values used in this research were introduced by Bertoldi, Decanini, and Gavarini (1993). The width of the equivalent strut can be calculated as follows:

$$\omega = \left(\frac{k_1}{\lambda_h} + k_2\right) d \tag{1}$$

Where d is the diagonal length of the infill panel, in m (Figure 6a), and λ_h is the relative stiffness coefficient, computed as follows:

$$\lambda_h = \sqrt[4]{\frac{E_m\, e \sin(2\,\theta)}{4 E_c\, I_{col}\, h_m}}\, h \tag{2}$$

Where E_m is the elastic equivalent modulus corresponding to the complete cracking stage on the infill, in kN/m^2; *e* is the thickness of the infill panel, in m; θ is the angle whose tangent is the infill height-to-length aspect ratio, in rad; E_c is the expected modulus of elasticity of the frame material, in kN/m^2; I_{col} is the moment of inertia of the columns, in m^4; h_m is the height of the infill panel, in m; and *h* is height of the column measured between centre lines of the beams, in m (see Figure 6a).

According to Decanini et al. (2004), the stiffness of the equivalent strut (k_{fm}) corresponding to the complete cracking stage is given by Equation (3), see Figure 6b:

$$k_{fm} = \frac{E_m\, e\, \omega}{d} \tag{3}$$

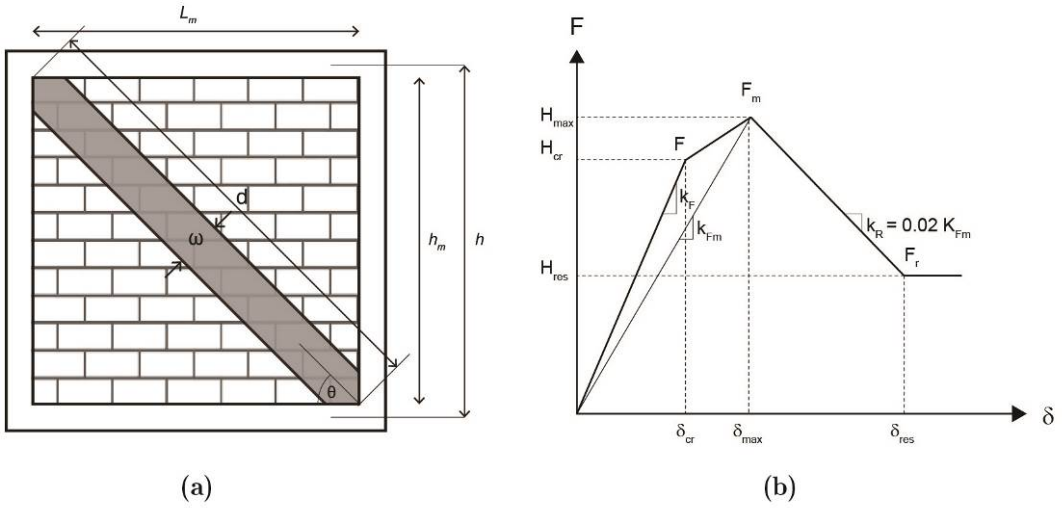

Figure 6. Equivalent Strut Method: (a) geometric characteristics of the equivalent diagonal strut for the ESM application, and (b) nonlinear relationship based on Decanini et al. (2004) and Sassun et al. (2016).

The resistance of the panel is simulated by an equivalent failure compressive strength (σ_{br}), which considers the different failure modes that could occur in both conventional tests and real structures subjected to seismic action. According to Decanini et al. (2004), four conventional failure modes have to be considered when computing the corresponding equivalent failure compressive stress: (a) diagonal tension, $\sigma_{br(1)}$, (b) bed-joint sliding, $\sigma_{br(2)}$, (c) crushing in the corners in contact with the frame, $\sigma_{br(3)}$, and (d) diagonal compression, $\sigma_{br(4)}$. The following Equations (4-7) indicates how to evaluate the equivalent failure compressive stress values according to the four conventional failure modes:

$$\sigma_{br\,(1)} = \frac{0.6\,\tau_{m0} + 0.3\,\sigma_o}{\omega/d} \tag{4}$$

$$\sigma_{br\,(2)} = \frac{(1.2\sin\theta + 0.45\cos\theta)\,f_{sr} + 0.3\,\sigma_o}{\omega/d} \tag{5}$$

$$\sigma_{br\,(3)} = \frac{(1.2\sin\theta + 0.45\cos\theta)\,f_{sr} + 0.3\,\sigma_o}{\omega/d} \tag{6}$$

$$\sigma_{br\,(4)} = \frac{1.16\,\sigma_{mo}\;0.3\,\tau_{m0}}{k1 + k2\,\lambda_h} \tag{7}$$

Where, σ_{m0}. is the vertical compression strength measured on masonry specimens, in kN/m^2; τ_{m0} is the shear strength measured with the diagonal compression test, in kN/m^2; f_{sr} is the slide resistance in the joints measured from the triplet test, in kN/m^2; and σ_0 is the vertical stress due to working loads, in kN/m^2. Once the equivalent failure compressive stress of the different failure modes have been determined, the minimum value $(\sigma_{br})_{min}$ defines the most probable failure mode of the infill. The lateral strength of the equivalent strut is given eventually by Equation (8):

$$H_{max} = (\sigma_{br})_{min}\, e\omega \tag{8}$$

The nonlinear deformation acceptance criteria of the equivalent strut was determined according to Decanini et al. (2004) and Sassun et al. (2016). Figure 6b shows the proposed load-deformation law constituted by four branches. A first linear elastic one corresponds to the uncracked stage (H_{cr}), and it is followed by a post-cracking phase up to the maximum strength (H_{max}), where F_m corresponds to the complete cracking stage of the infill panel. The third descending branch of the curve describes the post-peak strength deterioration of the infill until it reaches the residual strength H_{res} and displacement δ_{res}. According to Sassun et al. (2016), the drift ratios of the constitutive law can be assumed as δ_{cr} = 0.1%, δ_{max}= 0.2%, δ_{res}= 0.8% which correspond to the damage state of a slender infill panel based on experimental results.

The ESM models the strut by using linear elastic elements that are pin-connected to the surrounding frame. The nonlinear behaviour is introduced at the ends of the strut by using axial springs, containing the load-deformation laws of the panel shown in Figure 7b. The Pombalino and *quincha* infilled models were calibrated following the described ESM approach by incorporating the equivalent struts to the already calibrated bare frame models.

The width of the equivalent strut of the infilled Pombalino frame was calculated as 0.21 m after applying Equation 1, and considering the parameters listed in Table 1. Figure 7a-b shows the

ESM configuration where the strut is highlighted in red and the axial springs in green. The stiffness coefficient λ_h was calculated as 12.325, considering coefficients $k_1 = 0.47$ and $k_2 = 0.04$, and the linear stiffness of the panel (k_{fm}) was calculated as 49740 kN/m by applying Equation (3).

Table 1. Parameters for the estimation of the equivalent strut of the infilled Pombalino frame.

h	1.9	[m]
h_m	1.74	[m]
E_c	10000000	[kN/m^2]
E_m	5500000	[kN/m^2]
e	0.12	[m]
I_{col}	0.00000512	[m^4]
d	2.52	[m]
Θ	0.763	rad

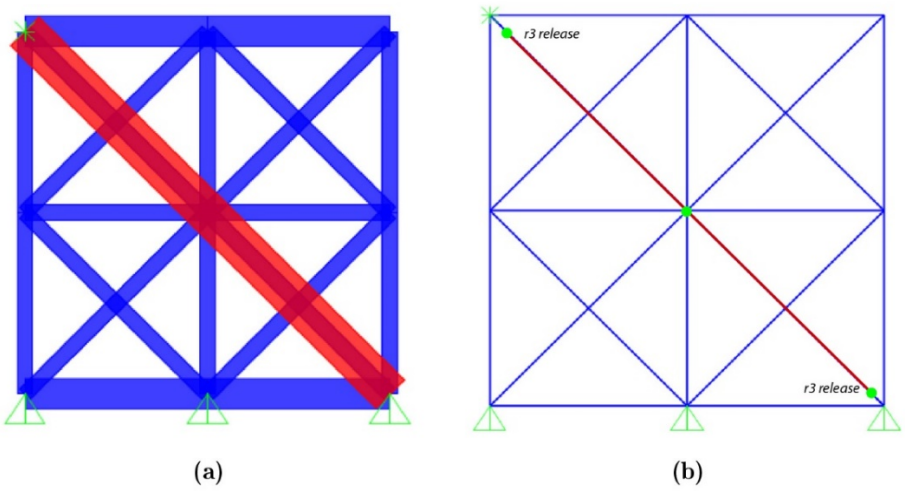

Figure 7. LPM based on ESM of the infilled Pombalino frame: (a) geometry and (b) infill hinges locations and DOF releases.

The equivalent failure stresses of the infill panel were calculated as follows: $\sigma_{br(1)} = 240.9$ kN/m^2; $\sigma_{br(2)} = 13119$ kN/m^2; $\sigma_{br(3)} = 5887.6$ kN/m^2; and $\sigma_{br(4)} = 8622.9$ kN/m^2, using the mechanical properties of masonry given by Poletti (2013). Given these results, a diagonal tension failure was predicted for the panel and the maximum lateral strength was calculated as 5.65 kN, see Figure 8a. Nonlinear axial springs were added at each node where the strut meets the frame, i.e., at the centre and the ends. Further details about calculations are reported in Jiménez (2021).

Figure 8b compares the numerical and experimental load-displacement capacity curves of the Pombalino infilled frame. A good agreement in terms of global stiffness is observed, and the maximum capacity is slightly underestimated by the model. Nonlinearities appeared at a global displacement of 0.015 m, when the axial springs of the struts reached their maximum capacity. After this phase, such springs moved to the post-cracking branch, until one of them reached its ultimate capacity at a displacement of 0.073 m. The axial springs of the diagonals in compression reached their maximum capacity at the global displacement of 0.018 m, followed by a progressive failure of the rotational hinges of the main frame, as shown in Figure 8c. This prediction is consistent with the experimental evidence. The diagonals separated from the main frame inducing a first loss of capacity followed by the collapse of the external half-lap connections. The analysis stopped when some of the rotational hinges reached their ultimate capacity and no longer worked.

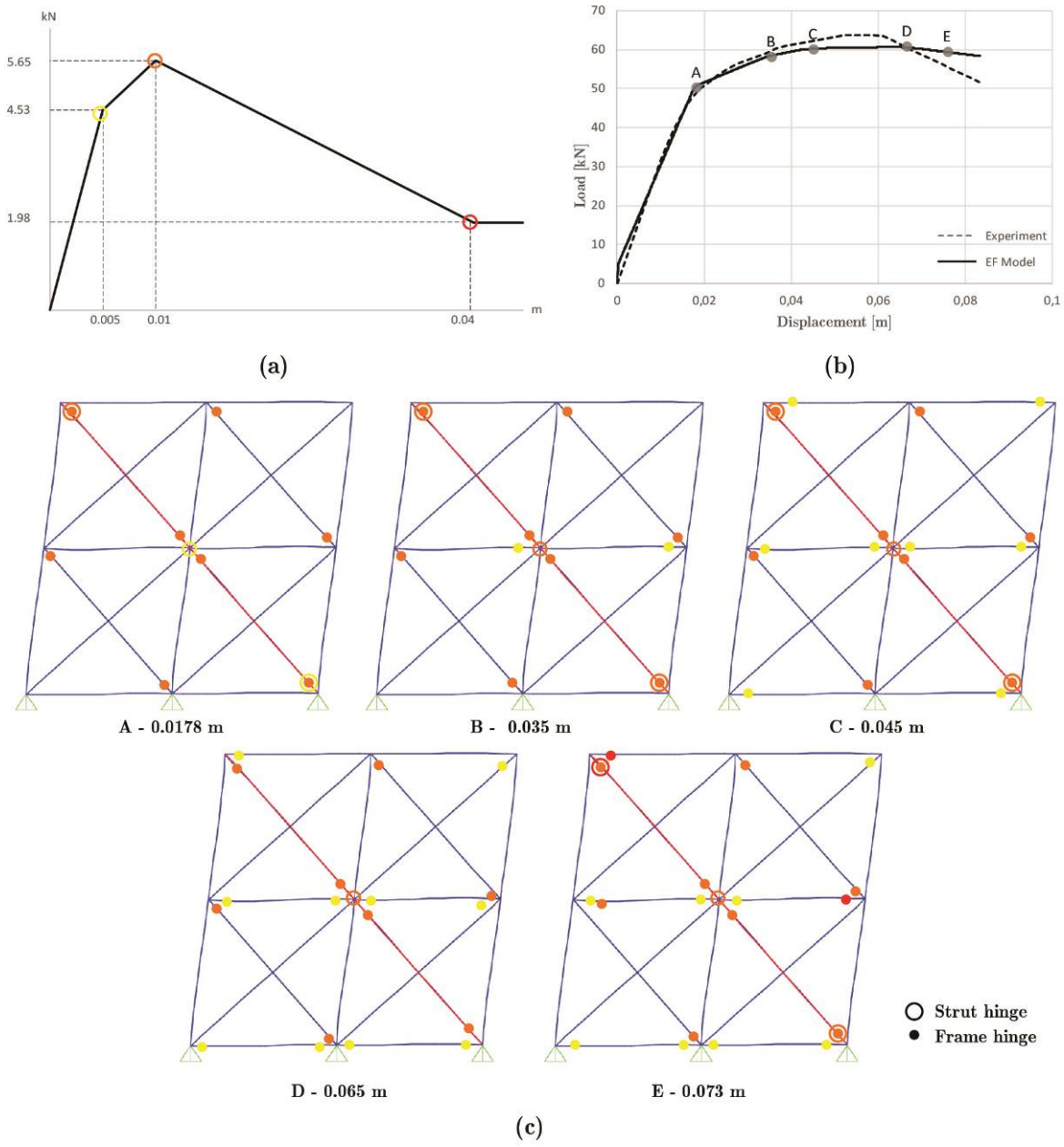

Figure 8. LPM based on ESM of the infilled Pombalino frame: (a) nonlinear load-displacement relationship of the equivalent strut, (b) numerical vs experimental capacity curves, and (c) evolution of the collapse mechanism.

Figure 9a shows the LPM model of the *quincha* frame tested by Moore and D'Ayala (2011), built in half-scale dimensions, with the ESM configuration. The width of the equivalent strut, highlighted in red, was calculated as 0.228 m wide by using the parameters listed in Table 2. The linear stiffness (k_{fm}) of the strut was computed as 1798 kN/m by applying Equation (3). The

mechanical properties of the adobe infill provided by the authors of the experiments were used to determine the equivalent failure compressive modes of the panel $\sigma_{br(1)} = 77{,}37$ kN/m^2, corresponding to the diagonal tension. The maximum lateral strength H_{max} was calculated as 1.418 kN, see Figure 10a.

Table 2. Parameters for the estimation of the equivalent strut of the infilled half-scale Quincha frame.

h	1.76	[m]
h_m	1.64	[m]
E_c	6400000	[kN/m^2]
E_m	200000	[kN/m^2]
e	0.08	[m]
I_{col}	0.00000144	[m^4]
d	81.45	[m]
Θ	0.96	rad

(a) (b)

Figure 9. LPM based on ESM of the infilled half-scale *Quincha* frame (a), and view of the specimen during the experiment (b) from Quinn (2015).

Figure 10b shows the comparison between the numerical and the experimental capacity curves, with a good agreement in terms of global stiffness and capacity. Figure 10c shows the collapse mechanism predicted by the model, which are consistent with what occurred in the experiment.

Firstly, the springs of the strut reached their maximum capacity at a displacement of 0.002 m and 0.007 m (instances A and B of Figure 10b). After that, the axial springs of the diagonal and some rotational hinges at the top post-beam connection reached their maximum capacity (instances B to E of Figure 10b). The collapse of the frame occurred at a global displacement of 0.04 m, when the top spring of the diagonal reached its ultimate capacity. From this point on, the differences between the experimental and numerical behaviour can be attributed to the simplified modelling strategy to represent the infill, which cannot represent the progressive critical local failures in detail.

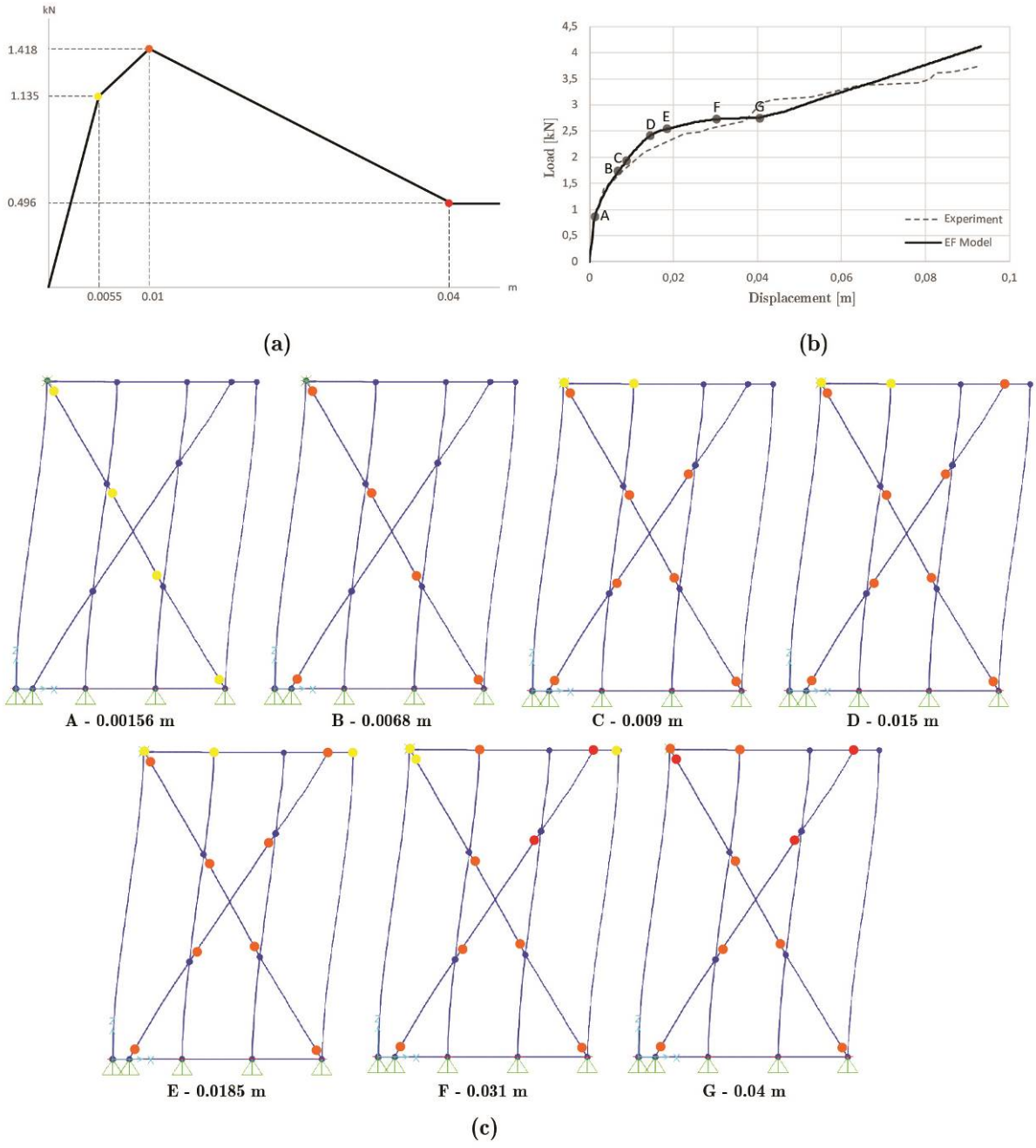

Figure 10. LPM based on ESM of the infilled half-scale *Quincha* frame: (a) nonlinear load-displacement relationship of the equivalent strut, (b) numerical vs experimental capacity curves, and (c) evolution of the collapse mechanism.

The last benchmark experimental results consists in a full-scale *quincha* frame tested by Torrealva, Vicente, and Michiels (2018), also studied by Perrone (2011), see Figure 1e. Figure 11a shows the discretization of the frame according to the LPM, with the infill represented by the ESM. As in the previous cases, the timber elements were modelled using frame elements with elastic

parameters, based on the mechanical properties of the *Moena Alcanfor* timber, as reported in Perrone (2011). Vertical post and horizontal beam elements had a cross-section of 0.08 × 0.06 m^2, while the diagonal member had a cross-section of 0.03 × 0.09 m^2. Vertical posts and horizontal beams were connected by mortise-and-tenon joints, while the diagonal was nailed to the beams and posts (Figure 11b-c).

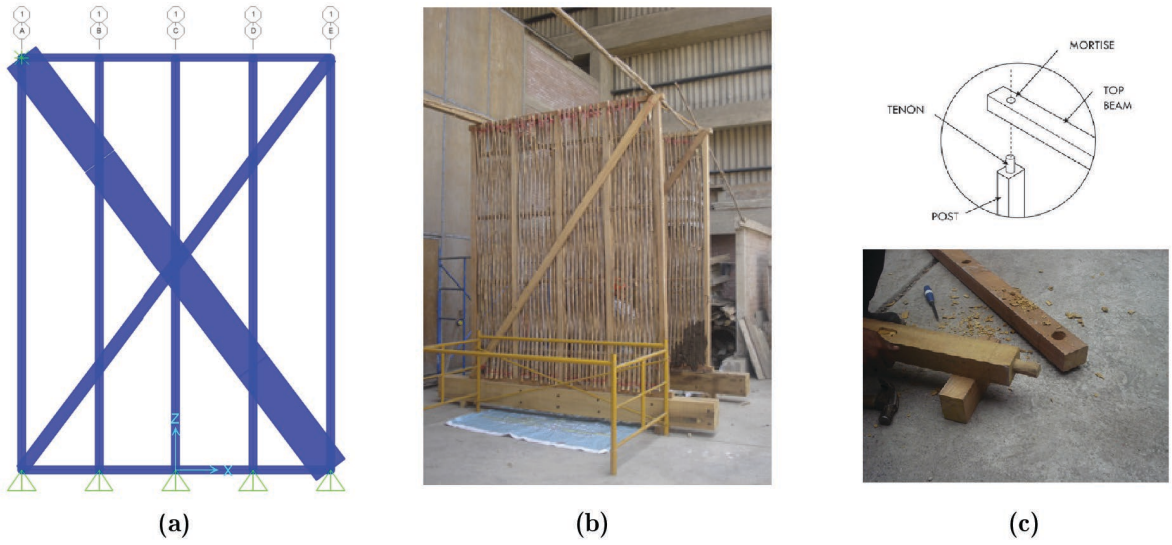

Figure 11. Model based on ESM of the full-scale infilled *quincha* frame (a), and view of the specimen (b) from Torrealva et al. (2018), with detail of the mortise-and-tenon connection (c).

The nonlinear behaviour of nailed connections was calibrated by using the empirical model developed by Chui and Ni (1997) to estimate the load-embedment capacity, according to Equation (9), see Figure 12. This model, based on the original proposal by Foschi (1974), was later modified to introduce the strength degradation effects:

$$P = (P_0 + K_1|\delta|)\left(1 - e\,(-\frac{K_0|\delta|}{P_0})\right) - (K_1 - K_2)(|\delta| - |\delta_P|)H(|\delta| - |\delta_P|) \qquad (9)$$

Where P is the load per unit length at embedment deformation δ, in N; P_0 is a parameter model denoting the intercept of the first asymptote, in N/mm; K_0 is the initial stiffness, in N/mm^2; K_1 is the slope of the first asymptote line, in N/mm^2; K_2 is the slope of the second asymptote line, in N/mm^2; δ_p is the deformation at ultimate strength, in mm, and; H ($|\delta|$-$|\delta_p|$) is the step function expressed in Equation (10):

$$H(|\delta| - |\delta_P|) = \begin{cases} 1 & \text{for } |\delta| - |\delta_P| \geq 0 \\ 0 & \text{for } |\delta| - |\delta_P| < 0 \end{cases} \quad (10)$$

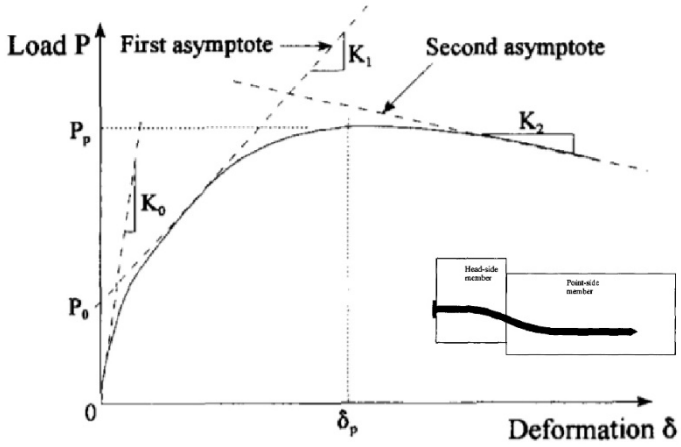

Figure 12. Load-embedment model for nailed connections by Chui and Ni (1997).

The diagonal was connected to the beam with four nails, and to the post with three nails. Therefore, two particular models had to be defined for each connection. Due to the lack of experimental data on these specific connections, a benchmark experiment on a nailed connection subjected to shear loads (Xu 2006) was used to estimate the load-embedment capacity of the nails to be used within the model, in agreement with Perrone (2011). The following initial parameters were extracted from the experiment to calculate the load-embedment relationship: P_0 = 1.2 kN/mm; K_0 = 0.66 kN/mm^2, P_p = 1.25 kN; δ_0 = 0.53 mm, K_1 = 0.0059 kN/mm^2; K_2 = 0.0013 kN/mm^2 δ_P = 10 mm. Sensitivity analyses were performed to adjust these values for the three and four nailed connections, by increasing P_0 until obtaining a good agreement between the model and the experiment. A higher load per unit length value (P) was assumed for the four nails connection respect to the three nails, in a ratio of 4:3. The initial stiffness (K_0) of each connection was calculated considering a displacement δ_0 of 3 mm. The load-embedment curves of the four nail-connections were characterised eventually by the following parameters: P_0 = 21 kN, K_0 = 12.42 kN/mm^2, K_1 = 0.023; K_2 = -0.02 kN/mm^2, and δ_P = 10.4 mm. As for the three nail-connections, the parameters were P_0 =12,8 kN; K_0 = 7.57 kN/mm^2,

$K_1 = 0$; $K_2 = -0.072$ kN/mm^2, and $\delta_P = 10.4$ mm. Figure 13a-b show the load-deformation relationships of both the four nail and three nail-connections, as they were implemented in the LPM of this study.

Perrone (2011) studied the nonlinear behaviour of the mortise-and-tenon connection of the full-scale *quincha* frame by developing a numerical micro-model. Her results in terms of moment-rotation relationship were used to characterize the nonlinear behaviour of this type of connection in the LPM of the present study. Rotational hinges were introduced at each post-beam connections, with the constitutive behaviour presented in Figure 13c.

Figure 13d shows the nonlinear behaviour of the infill through the ESM. The equivalent width of the strut was 0.369 m, calculated by considering the parameters listed in Table 3. The equivalent failure modes of the frame were estimated based on the mechanical properties of the adobe, where the most probable failure mode of the panel is the diagonal tension, $\sigma_{br(1)} = 93.145$ kN/m^2 .The maximum lateral strength H_{max} of the panel was calculated as 2.75 kN. The above results were employed to define the load-displacement relationship controlling the ESM, as shown in Figure 13d.

Table 3. Parameters for the estimation of the equivalent strut of the full-scale infilled quincha frame.

h	3.14	[m]
hm	3.08	[m]
Ec	12000000	[kN/m^2]
Em	200000	[kN/m2]
e	0.08	[m]
Icol	0,0000014	[m^4]
d	4.06	[m]
Θ	0.90885	rad
λh	9.21302	-

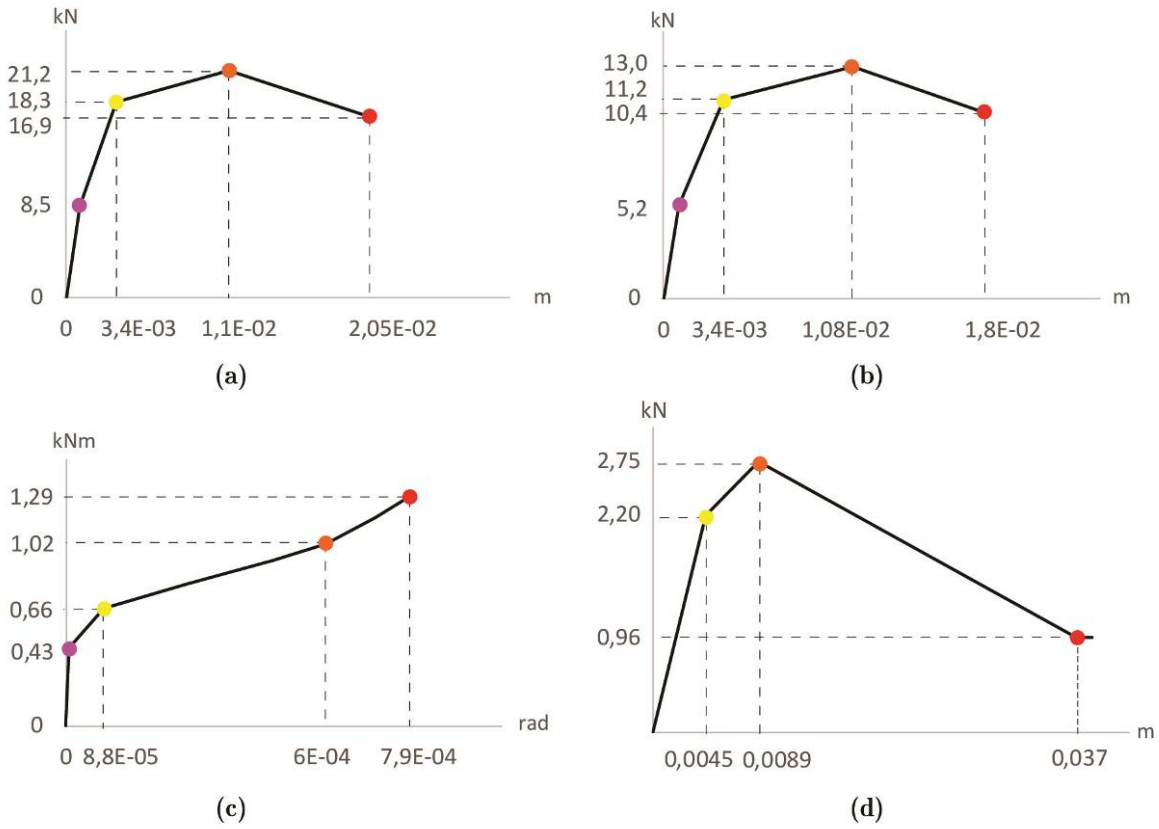

Figure 13. LPM based on ESM of the full-scale infilled *Quincha* frame: load-deformation relationships of (a) four and (b) three nail-connections, (c) mortise-and-tenon joint, and (d) equivalent strut.

Figure 14a shows the comparison between the experimental and numerical load-displacement capacity curves, denoting a good agreement in terms of global stiffness and ultimate capacity. The model reached a maximum load of 12.4 kN at a displacement of 0.092 m. The global stiffness of the model is 869 kN/m, slightly higher than that obtained in the experiment. The collapse mechanisms predicted by the model revealed that the axial springs of the strut and diagonal elements plasticized first, as shown in Figure 14b (instances A-B of Figure 14a). Subsequently, some of the springs of the diagonal reached their maximum capacity at a displacement of 0.026 m (instance B of Figure 14a). Afterwards, some of the rotational hinges at the top and bottom connections of the frame entered in the plastic range (instances C-D of Figure 14a). The diagonal failed when one of the central springs reached its ultimate capacity (instance E of Figure 14a). After this stage, only the rotational hinges continued working in the model. This response was in good agreement with the experiment in terms

of both local failures and global mechanism, since the stiffness of the experimental frame reduced after a central nailed connection failed, but it maintained its stability given the high ductility of the mortise-and-tenon joints.

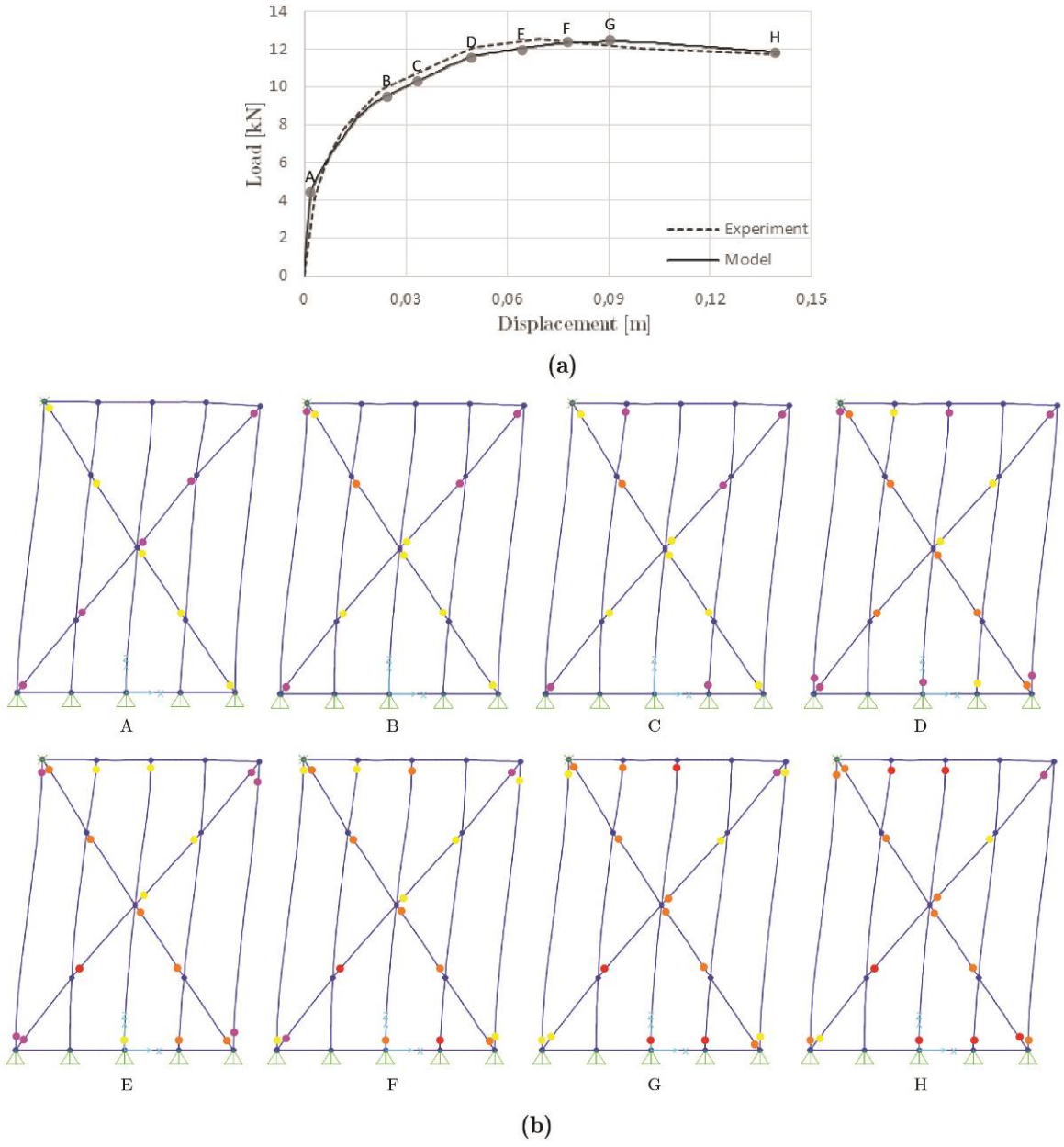

Figure 14. LPM based on ESM of the full-scale infilled *Quincha* frame: (a) numerical vs experimental capacity curves, and (b) evolution of the collapse mechanism.

2.3 Numerical simulation of experiments on unreinforced masonry walls

Three experimental programs on masonry walls were considered for simulation, including both the in-plane (Augenti et al. 2011) and out-of-plane behaviour (Gazzola 1985, Griffith and Vaculik 2007).

A FE continuum macro-mechanical modelling approach was adopted to analyse the structural behaviour of masonry subjected to in-plane and out-of-plane actions. A two-dimensional nonlinear material model was used for shell element applications. This model is based on the theories of Darwin-Pecknold (Darwin and Pecknold 1974, 1977) and Vecchio-Collins (Frank J. Vecchio and Collins 1986), which represent the cracking by means of a fracture energy-based approach with softening behaviour (CSI 2016), according to the Total Strain Crack model (Vecchio and Collins 1993, Reinhardt 1984, and Hordijk 1991). A co-axially rotating smeared crack model considers both cracking and crushing of the material. This model is considered appropriate for the applications to quasi-brittle materials like concrete and masonry.

Figure 15a shows the first benchmark example consisting in the in-plane loaded wall tested by Augenti et al. (2011). The wall was modelled using layered shell elements with a mesh of approximately 0.20×0.28 m^2, with a total number of 258 finite elements. The section of the element was defined with only one layer of 0.31 m thickness, and four integration points along the thickness direction. All the nodes at the base of the model were restrained in all the translational DOFs simulating the rigid support conditions of the experiment. A vertical pre-compression of 200 kN was applied at each pier of the wall, followed by an incremental lateral displacement applied at a height of 3 m on the left side of the wall.

The masonry material was defined as a nonlinear for all its three membrane stress components, σ_{11}, σ_{22} and σ_{12}. The constitutive law considered an isotropic material with Young's modulus E = 2.22 GPa and Poisson's ratio $\nu = 0.2$. The stress-strain nonlinear deformation relationships are shown in Figure 15a-b, being the compressive strength f_c = 3.96 MPa. The

compressive part of the uniaxial stress-strain curve, represented by a parabolic law (Figure 15b), was finally determined considering the analytical model proposed by Turnšek and Sheppard (1998), and Kaushik, Rai, and Jain (2007). The tensile behaviour of masonry (Figure 15c) was defined considering a linear response until the peak tensile stress (f_t), which was estimated as 3.5% of the masonry compressive stress (0.135 MPa). The strain at the peak tensile stress (ε'_t) was assumed as 0.06‰, after executing sensitivity analyses. A higher compressive strain deformation capacity is required to achieve greater deformations of the model without increasing the strength capacity. According to D'Ambra, Lignola, and Prota (2016), this behaviour was obtained by incrementing artificially the peak strain value, as shown in Figure 15b (dashed line). This simplification allowed the model to reproduce correctly the rocking behaviour due to the base rotation of the piers in the experiment. An alternative approach to reproduce correctly the test results by advanced numerical simulation is addressed in-depth in Saloustros et al. (2017a).

Shear strength of masonry is computed from the axial stress-strain relationship introduced in SAP2000, by using a conventional Coulomb friction model. According to D'Ambra, Lignola, and Prota (2016), a friction angle equal to 23º was used to define the shear model, as also recommended by Eurocode 6 (CEN 2005) for masonry.

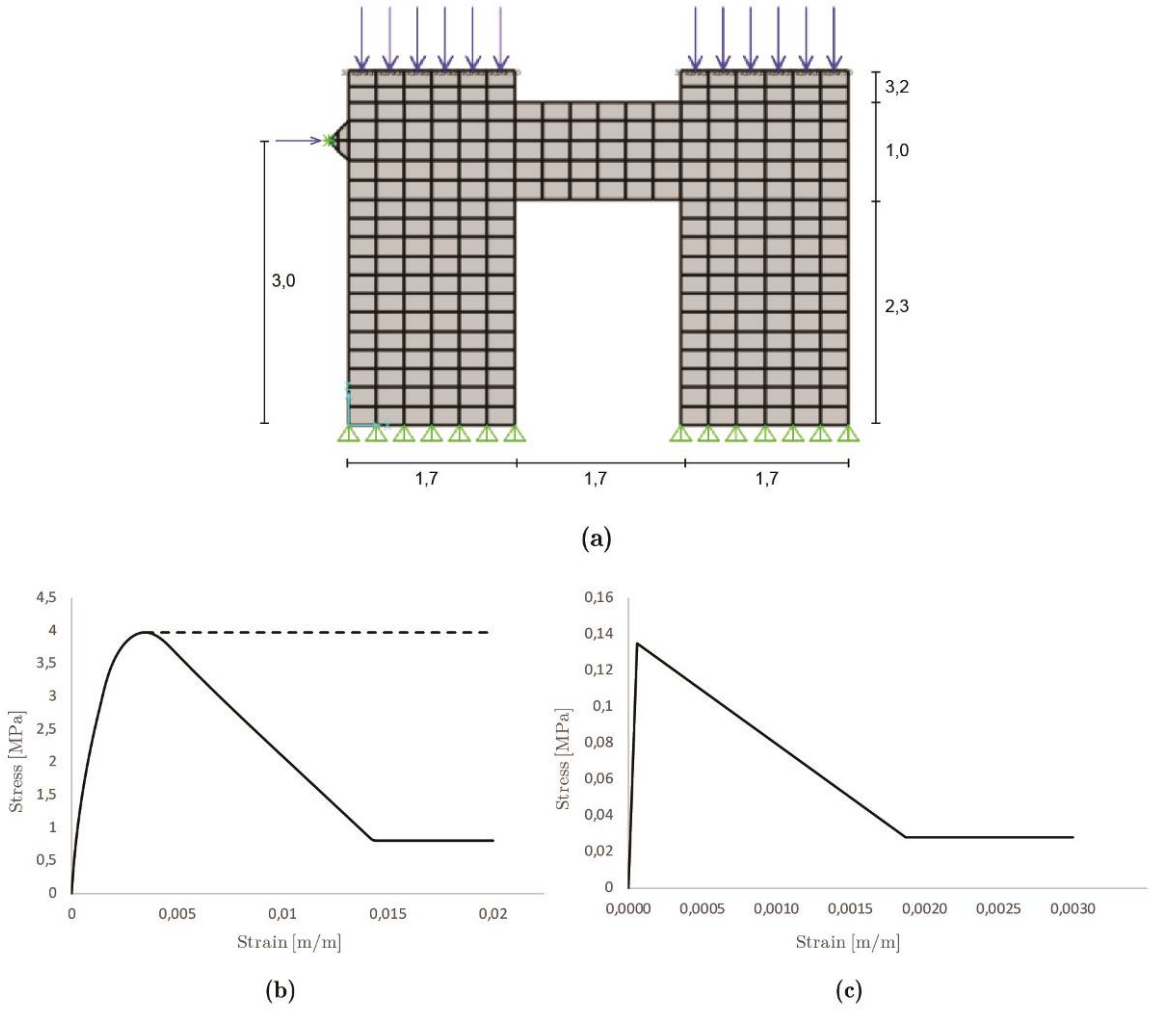

Figure 15. (a) FE model of the in-plane loaded masonry wall tested by Augenti et al. (2011) (dimensions in m), and b) stress-strain uniaxial relationships for masonry in compression and (c) tension.

Figure 16a displays the obtained load-displacement capacity curve, where the local failures occurring during the analysis are highlighted with the instances A to D. The results revealed a good agreement compared to the experiment in terms of global stiffness, maximum and ultimate capacity of the wall. The maximum capacity was 180.8 kN (0.4% error), while the initial stiffness was 4.35×10^4 kN/m (5.9% error).

Figure 16b shows the principal compressive stress contours corresponding to the ultimate displacement of the simulation, i.e., instance D in Figure 16a. This result revealed the formation of the resistant mechanism characterized by diagonal struts within the piers as well as in the central

spandrel, whereas significant compressive stress is registered at the base of the pier. Figure 16c shows the principal tensile strain contours indicating the development of the cracking damage at the ultimate displacement. Cracking at the centre of the spandrel and at the base of the piers appear at instance A, followed by diagonal cracking development in both spandrel and piers at instances B and C. After the wall reached its maximum strength at instance C, the stiffness of the frame slightly decreased, and the model could not capture the resistance drop of 15% observed in the experiment.

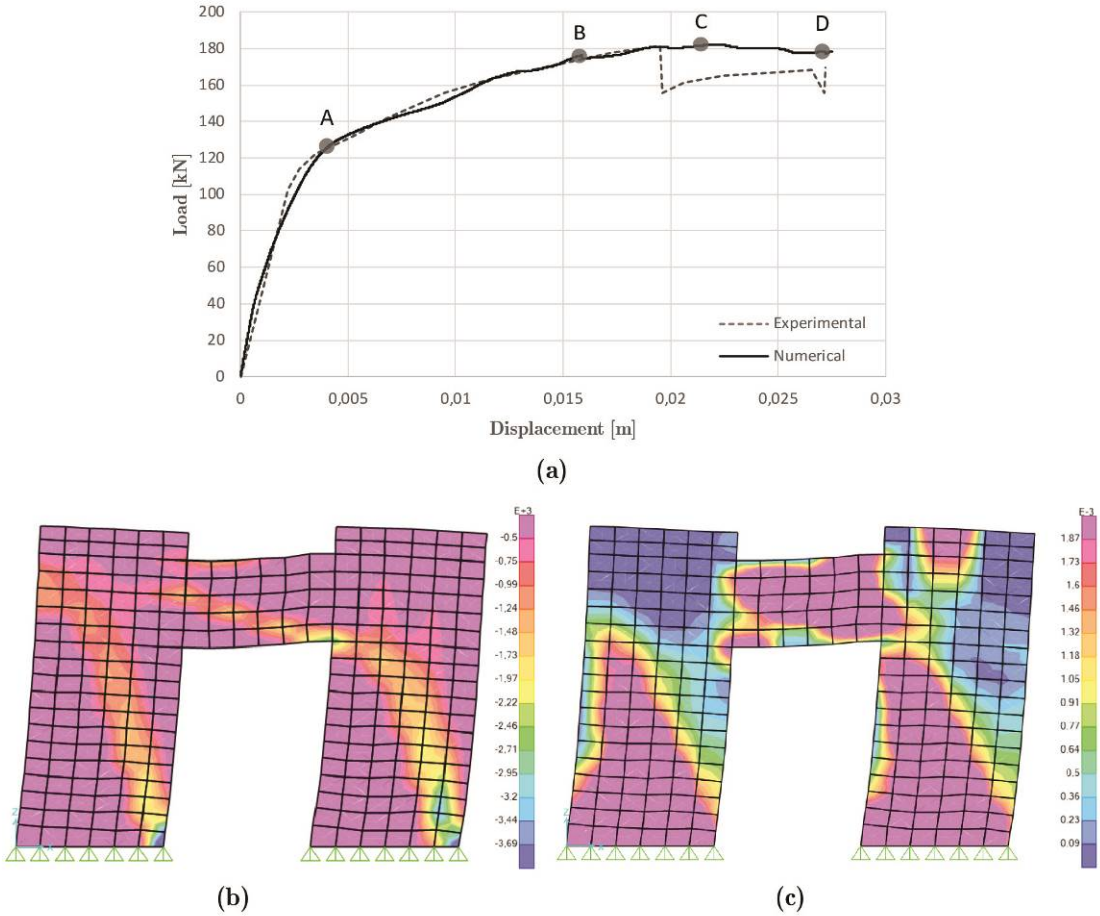

Figure 16. FE model of the in-plane loaded masonry wall tested by Augenti et al. (2011): (a) experimental vs numerical capacity curves, (b) principal tensile strain contour, and (c) principal compressive stress contour at the ultimate stage D of the analysis.

The second benchmark experiment consists in a URM wall tested under out-of-plane actions by Gazzola (1985), and subsequently analysed by Lourenço (2000). The wall was loaded until failure with increasing out-of-plane uniform pressure. Preliminary sensitivity analysis was performed to

study the influence of the mesh refinement and of the through-thickness integration points (IPs) on the nonlinear response of the model. Figure 17a shows that the models with less than 64 elements were not able to capture accurately the nonlinearities. However, very small differences in terms of initial stiffness and peak load were recorded by using different mesh sizes. Figure 17b shows a slight difference in terms of capacity between the 4 to 9 IPs models, whereas the increment from 9 to 18 IPs does not have a major influence on the out-of-plane response of the wall. The model showed the typical response of walls subjected to out-of-plane loads, where cracking started to appear at the mid-height of the bottom face of the panel, as shown in Figure 17c. According to Lourenço (2000), predominant cracking occurred in the shorter span direction of the panel up to the peak load, which corresponds to higher bending moments and lower tensile strengths. After the peak load, the typical yield-line type of collapse appears with marked softening lines, see Figure 17d. The results obtained are consistent with those shown in Figure 17e that were obtained by Lourenço (2000) at the ultimate pressure.

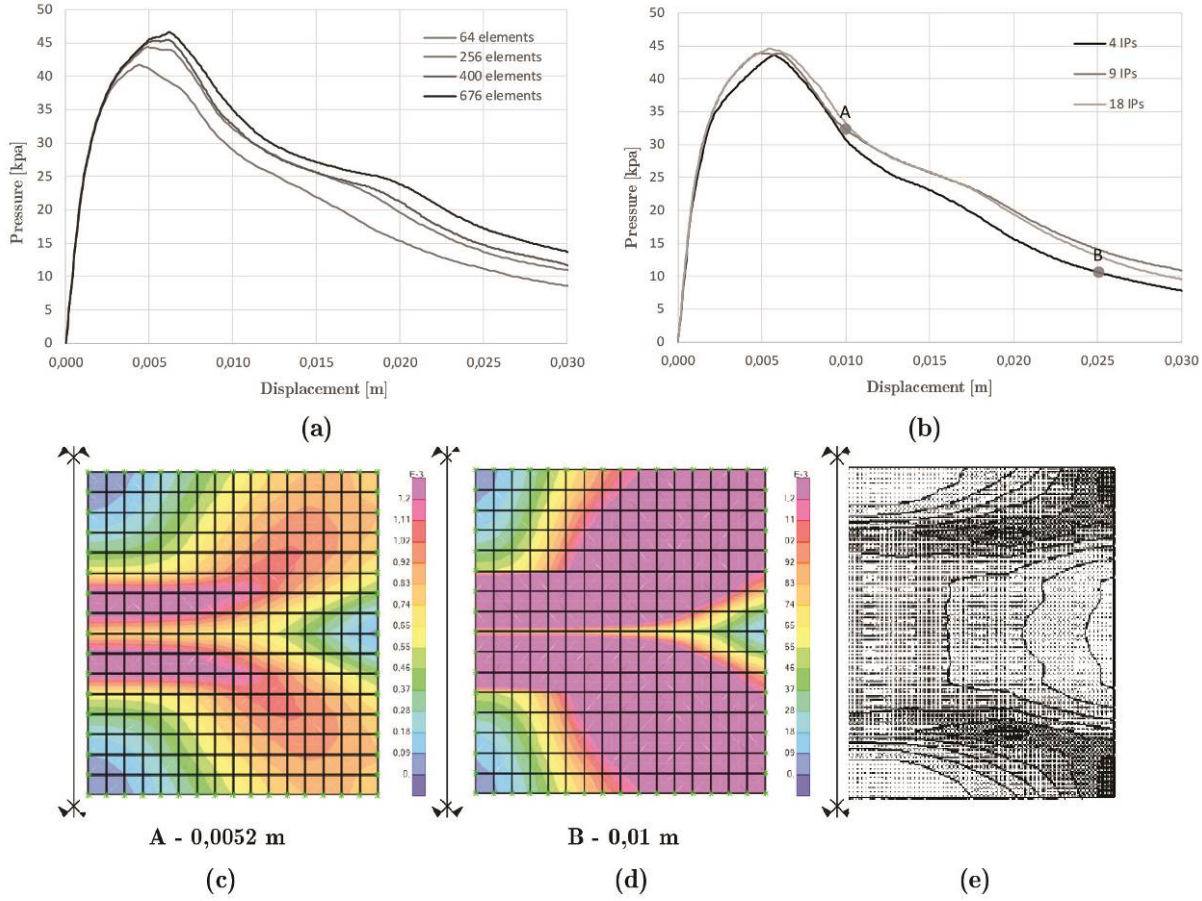

Figure 17. FE model of the out-of-plane loaded masonry wall tested by Gazzola (1985): sensitivity analyses considering (a) a mesh refinement in the model with 9 IPs, and (b) different IPs in the model of 676 elements. FE results of the wall: (c) principal strain contours in the bottom face at the peak load, and (d) post peak, and comparison with (e) plastic strain at the ultimate pressure obtained by Lourenço (2000).

The third benchmark experiment is the URM wall tested under out-of-plane actions by Griffith and Vaculik (2007). The study of Petracca et al. (2017) is also considered as a reference, as it provides an in-depth analysis of this complex experiment, by developing sophisticated computations based on micro-modelling and multi-scale modelling. Given the symmetrical layout of the wall, only the left part of it was modelled considering appropriate symmetrical boundary conditions, as shown in Figure 18a-d. The base and top edges of the panel were simply supported by fixing the out-of-plane DOFs. The vertical edge of the return wall was fixed in all the DOFs, and a symmetry axis along the right edge considered fixed horizontal translation, as well as the out-of-plane rotations.

The section of the wall is 0.11 m, set with two shell layers of 0.055 m thickness each, and a total of 10 IPs along the thickness direction. The masonry material was defined as nonlinear for all of the three membrane stress components of the layer, σ_{11}, σ_{22} and σ_{12}. A friction angle ϕ equal to 23º was considered to describe the shear model. A plastic stress-strain constitutive law defined the behaviour of the material model, with $E = 5.27 \times 10^7$ kN/m^2, Poisson's ratio $\nu = 0.2$, $f_t = 352$ kN/m^2, $f_c = 17600$ kN/m^2. The compressive behaviour of masonry was described by means of the analytical model of Kaushik, Rai, and Jain (2007), that is shown in Figure 18e. The tensile behaviour was represented by the bilinear stress-strain relationship shown in Figure 18f. The curve is composed by an elastic branch up to the maximum tensile strength f_t, defined as the 2% of f_c. The tensile fracture energy of the model G_f was set equal to 0.04 kN/m based on sensitivity analysis in order to find an agreement with experimental results. The residual tensile strength was set equal to 50% of f_t, see Figure 18f. Such rather high value was derived from a careful sensitivity analysis, as lower values for this parameter were not able to represent correctly the post-peak experimental behaviour. According to Griffith and Vaculik (2007), the definition of a proper post-peak strength plateau is meaningful for the case of simply supported out-of-plane loaded walls. Petracca et al. (2017) also highlighted an "apparent" plastic behaviour of the wall tested by Griffith and Vaculik (2007), with an almost constant post-peak strength plateau, as will be discussed in the following. Therefore, the assumed rather high value of the residual strength is motivated by the need of ensuring the correct redistribution of stresses after the peak load and the development of the mechanism with yield-line type of failure. A vertical pre-compression of 100 kPa was applied first at the top of the wall, followed by an out-of-plane pressure imposed to the outer surface of the main wall under displacement control. The deflection of the wall was measured at the centre of the wall, where the maximum displacement was expected, as shown in Figure 18d.

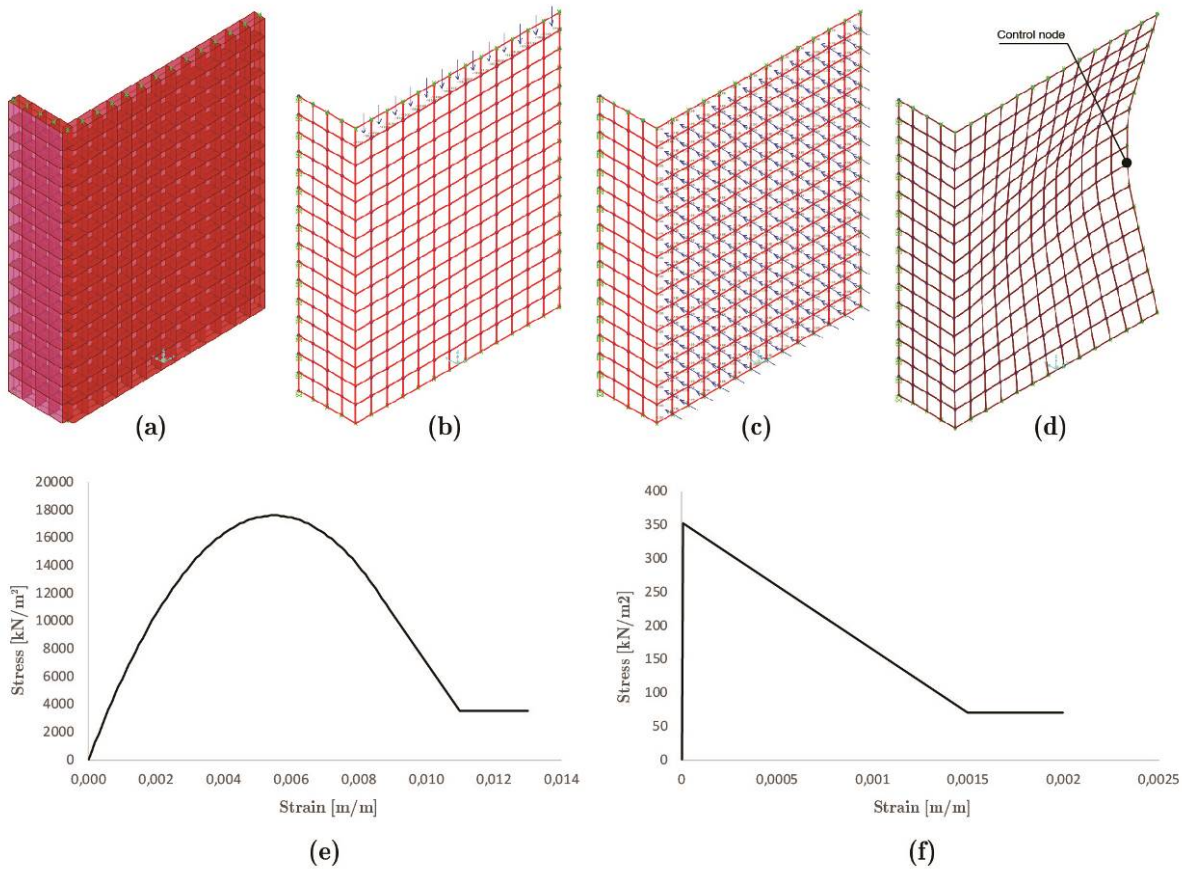

Figure 18. FE results of out-of-plane loaded masonry wall tested by Griffith and Vaculik (2007): (a) geometry, (b) surface pressure, (c) vertical pre-compression and (d) deformation. Assumed compressive (e) and tensile (f) stress-strain relationships of masonry material.

Figure 19a shows the comparison between the experimental and the numerically calibrated pressure-deflection curve, evidencing a very good agreement. Figure 19b-c show the evolution of the principal tensile strains during different stages of the analysis. At the peak capacity (instance A in Figure 19a), the model displays diagonal cracking developed an extensive damaged zone, together with a horizontal crack in the centre of the wall, in agreement with the experimental evidence. Vertical cracking occurs also at the intersections of the return walls with the front one. As discussed by Griffith and Vaculik (2007), and highlighted also by Petracca et al. (2017), the apparent post-peak plastic behaviour of the wall may be attributed to a full redistribution of bending moment along the diagonal cracks to horizontal bending along the vertical edges of the wall. The bending restraints exerted by

the return walls provided additional capacity against the transfer of load from the diagonal bending mechanism.

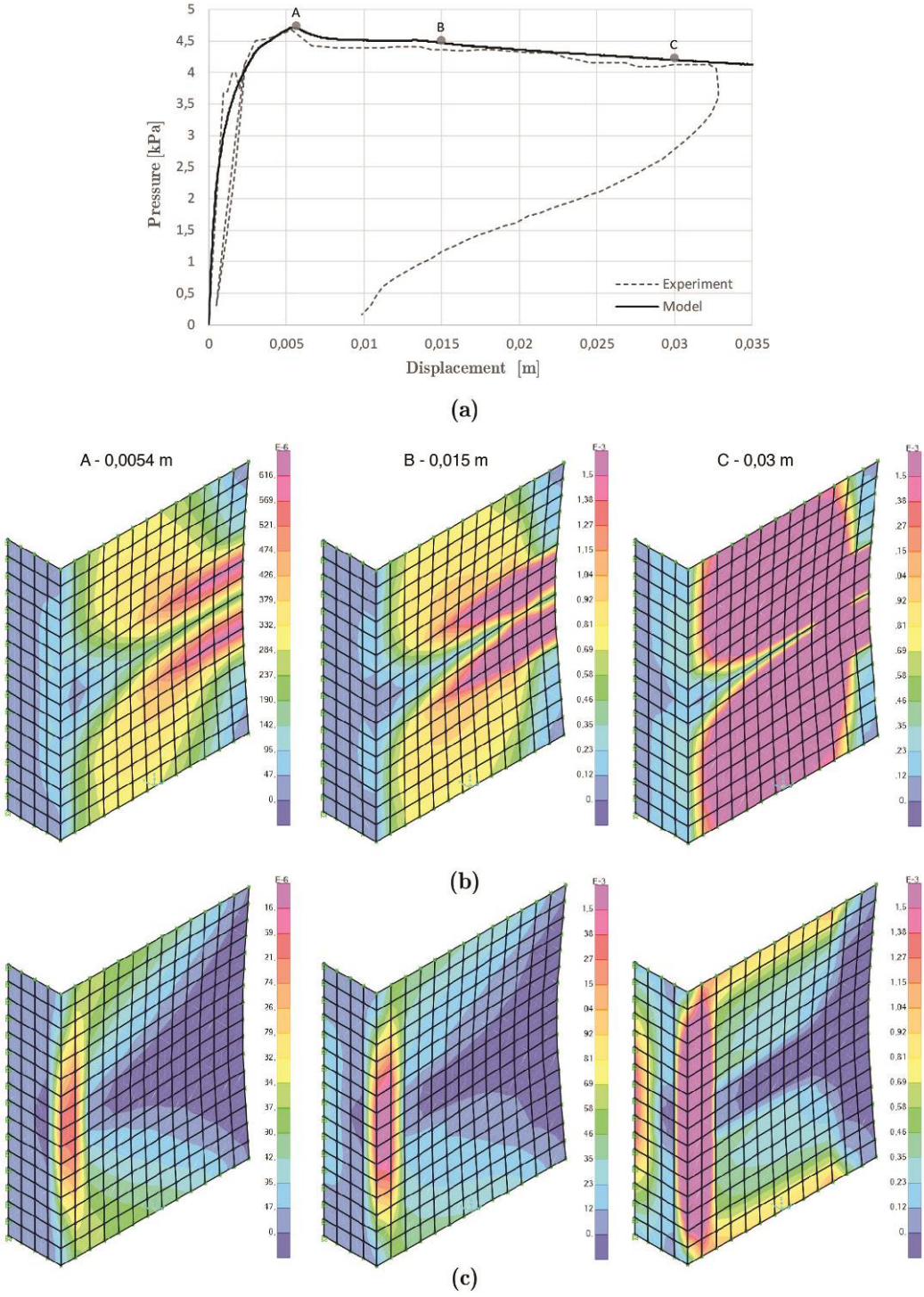

Figure 19. FE results of out-of-plane loaded masonry wall tested by Griffith and Vaculik (2007): (a) Experimental vs. numerical pressure-deflection curves, (b) principal tensile strain in the bottom and (c) top faces measured at different instances A, B and C.

It is worth noticing that more sophisticated computational strategies, like those adopted by Petracca et al. (2017), are certainly able to reproduce more accurately the experiments, thanks to their capability of modelling the complex behaviour of masonry even at the level of the interaction among the constituents (bricks and joints). However, the adopted simpler continuum FE model shows to be able to represent correctly the development of the failure mechanisms and the load-displacement response. For this reason, it can be concluded that the considered simplified approach can provide results that are worthy of consideration for the analysis of more complex existing buildings, like those presented in the following section.

.

3. Numerical modelling of hybrid timber–masonry buildings of Valparaíso, Chile

3.1 Description of the case-studies

The city of Valparaíso (Chile), listed in the World Heritage Site list by UNESCO, is composed of valuable historical buildings with hybrid structural systems, where timber frames and masonry walls coexist. Available documentation about the built environment in Valparaíso is scarce and fragmented, and detailed data are missing about the behaviour and characteristics of construction materials (timber, adobe, masonry) and structural details (e.g. carpentry joints). The need for systematic technical information has recently conducted to the development of research studies for survey and data collection (B. Jiménez, Pelà, and Hurtado 2018) aimed at the vulnerability assessment of the urban building stock (Jiménez, Saloustros, and Pelà 2021). The lack of experimental data about the mechanical behaviour of the specific structural systems in Valparaíso has also motivated the numerical approach followed in this work to calibrate the numerical models, which is based on careful comparisons with available experiments on timber frames and masonry walls of similar typologies (Pombalino and Quincha).

In this work, two representative buildings located in the historical *Cerro Alegre* neighbourhood were analysed under lateral loads using the simplified FE models previously

calibrated in Section 2. Both buildings are shown in Figure 20a-b and were designed and constructed using the timber *platform frame* system combined with URM walls, as reported by Jiménez (2015). The disposition of the structural elements, as well as the type of materials, connections, infill systems, and finishing are very similar in both buildings.

(a) (b)

Figure 20. Cases of study in the Cerro Alegre neighbourhood: (a) Building 1, located at 558 *Lautaro Rosas* street, and (b) Building 2, located at 167 *Paseo Dimalow* street, Valparaíso, Chile.

The traditional *platform frame* is composed of a light timber frame in which a storey platform is constructed at each floor, see Figure 21. The studs for the next floor are usually erected on this platform with an intervening beam. The frame walls are usually configured in Valparaíso by stud elements of 0.1×0.1 m^2 cross-section, spaced $0.4 \div 0.6$ m each, and distributed between the top and bottom horizontal beams. Diagonal braces are usually introduced every two studs, and they are located next to the openings. Traditional carpentry joints reinforced with nails are used to connect the timber elements, where mortise-and-tenon joints are used to connect vertical posts and horizontal beams, including the sills of the openings, and notched joints connect the diagonals with the main frame, as shown Figure 21 at the right. Adobe blocks of $0.50 \times 0.10 \times 0.08$ m^3 fill the external walls of the façade, while lath-and-plaster are used for the internal partitions. The joists of the storeys have 0.125×0.05 m^2 cross-section, and are separated every 0.4 m nailed over the beams of the frame or embedded into the masonry, as appropriate. Wooden boards of 0.10 m width and 0.01 m thickness,

nailed at the top and bottom of the joists, constitute the floors and ceilings. Rudimentary trusses are supported by the walls and form the roof, with inclined rafters shaping pitched roofs, with around 10% slope. Wooden ribbons over the trusses support the corrugated iron planks covering the roof structure.

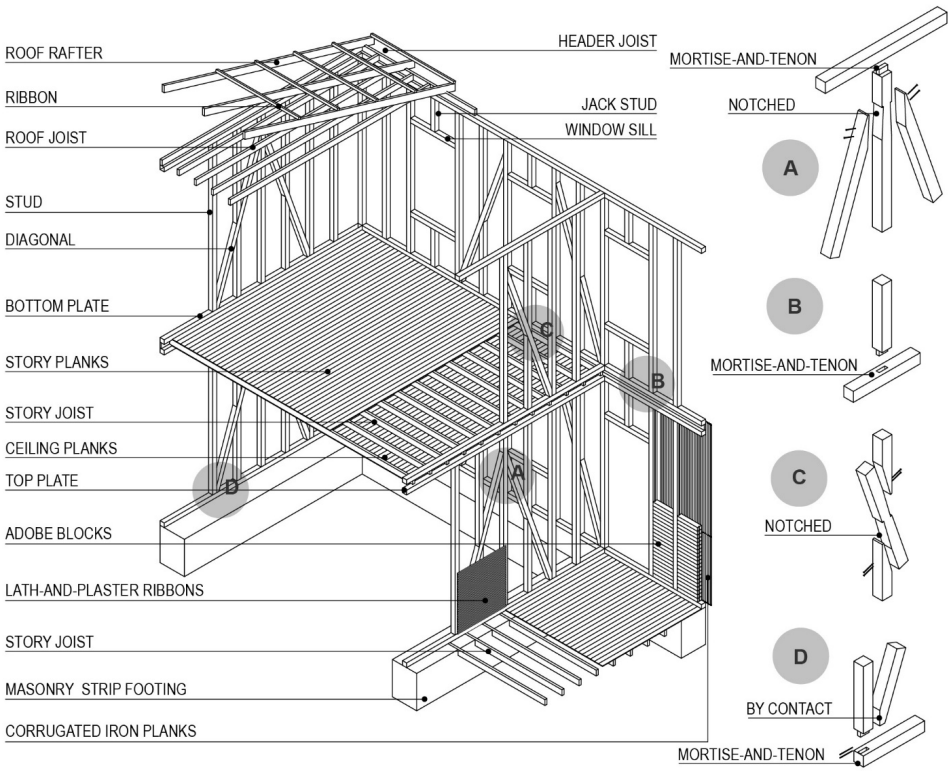

Figure 21. Isometric view of a representative timber *platform frame* system of Valparaíso.

As reported by Jiménez (2015), most of the timber elements are made of Oakwood and Oregon Pine wood in Valparaíso. In both structures analysed in this work, URM load-bearing sidewalls are connected to the timber frames at the storey levels. The walls are made of fired clay bricks of 0.38 × 0.195 × 0.06 m^3 and lime mortar, arranged in English bond. The sidewalls have variable thickness along the height, varying at each storey, ranging from 0.6 m to 0.2 m from the bottom to the top levels. The storeys are supported by joists commonly embedded or simply supported over the bricks. The sidewalls are not shared with the load bearing system of the adjacent buildings,

and they are placed only next to each other with the function of firewalls. The foundations under the load-bearing walls and timber frames are strip footings made of brick masonry, built on rocky soil, with 0.6 m thickness and 0.80 m height.

Building 1 corresponds to a three-storey building dating back to 1909, which was designed by the architect Juan Blezard, as revealed in the original drawings shown in Figure 22a-b. The building is located in the number 558 of the Lautaro Rosas street, with a central position in a building aggregate. The first and second levels of the building are 87.39 m^2, while the third level has the half of the built area and an exterior terrace. The structural system is composed of two main bays along

the longest direction of the building, which are divided by perpendicular internal partition walls distributing the rooms.

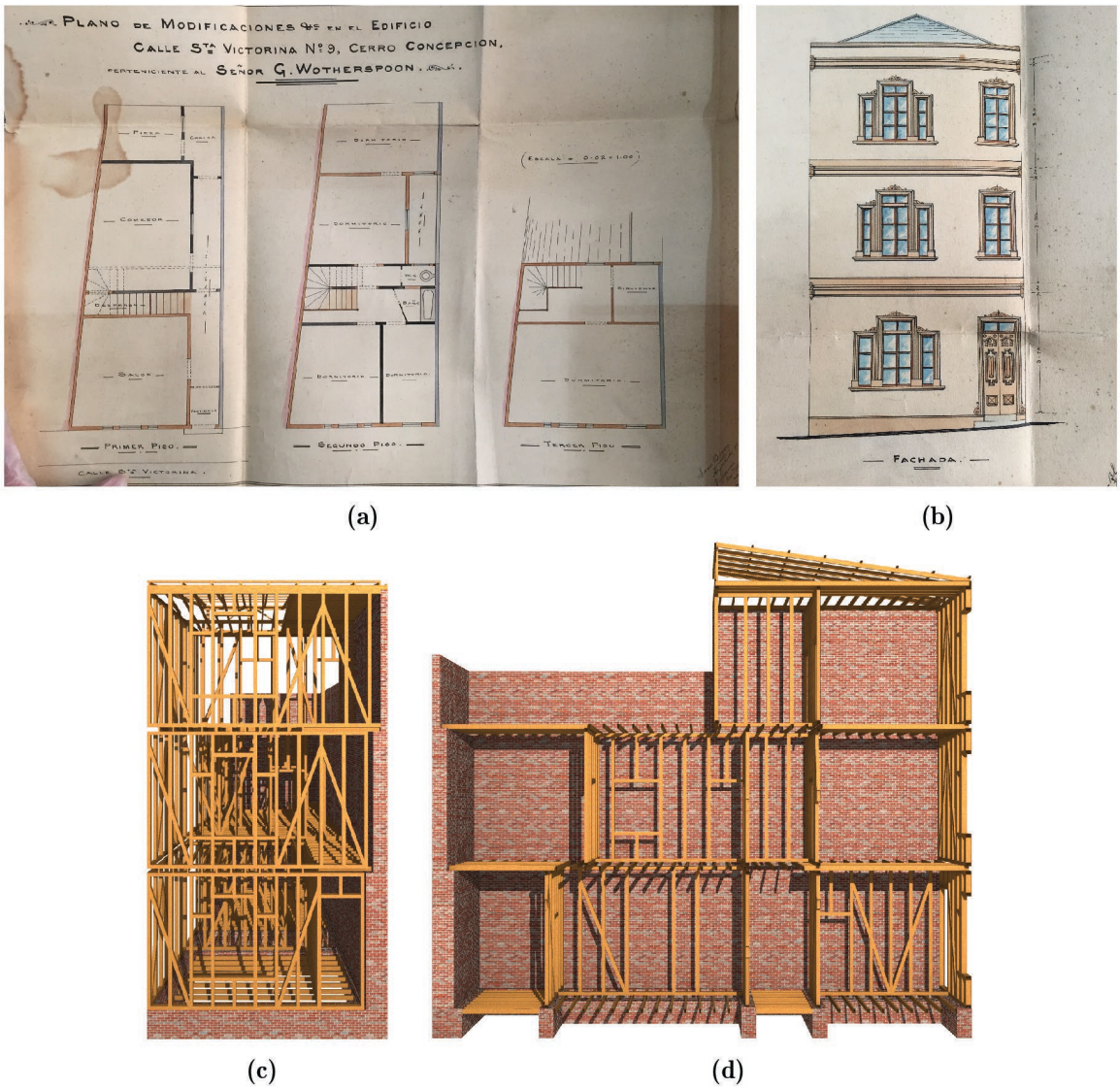

Figure 22. (a-b) Original drawings of Building 1 located in the number 558 of the Lautaro Rosas street in the Cerro Alegre. Source: *Registro Patrimonial de la Dirección de Obras Municipales de Valparaíso (DOM).* (c-d) Frontal and transversal section views showing the structural configuration of Building 1.

Building 2, shown in Figure 23, is a two-storey original house lately reformed for commercial use with a surface of 190 m^2. The available data about the building were gathered when it was under restoration. This fact permitted a complete and detailed on-site inspection of the constructive system. The building is located in the number 167 of the Paseo Dimalow street, having a central position in

an in-row aggregate of four buildings. The date of construction is unknown, but it was possible to recognize the building in cartographic drawings since 1879. The building presented regular shape both in plan an elevation. The structural system has three bays, where the main one corresponds to a central corridor in-between the different rooms of the building.

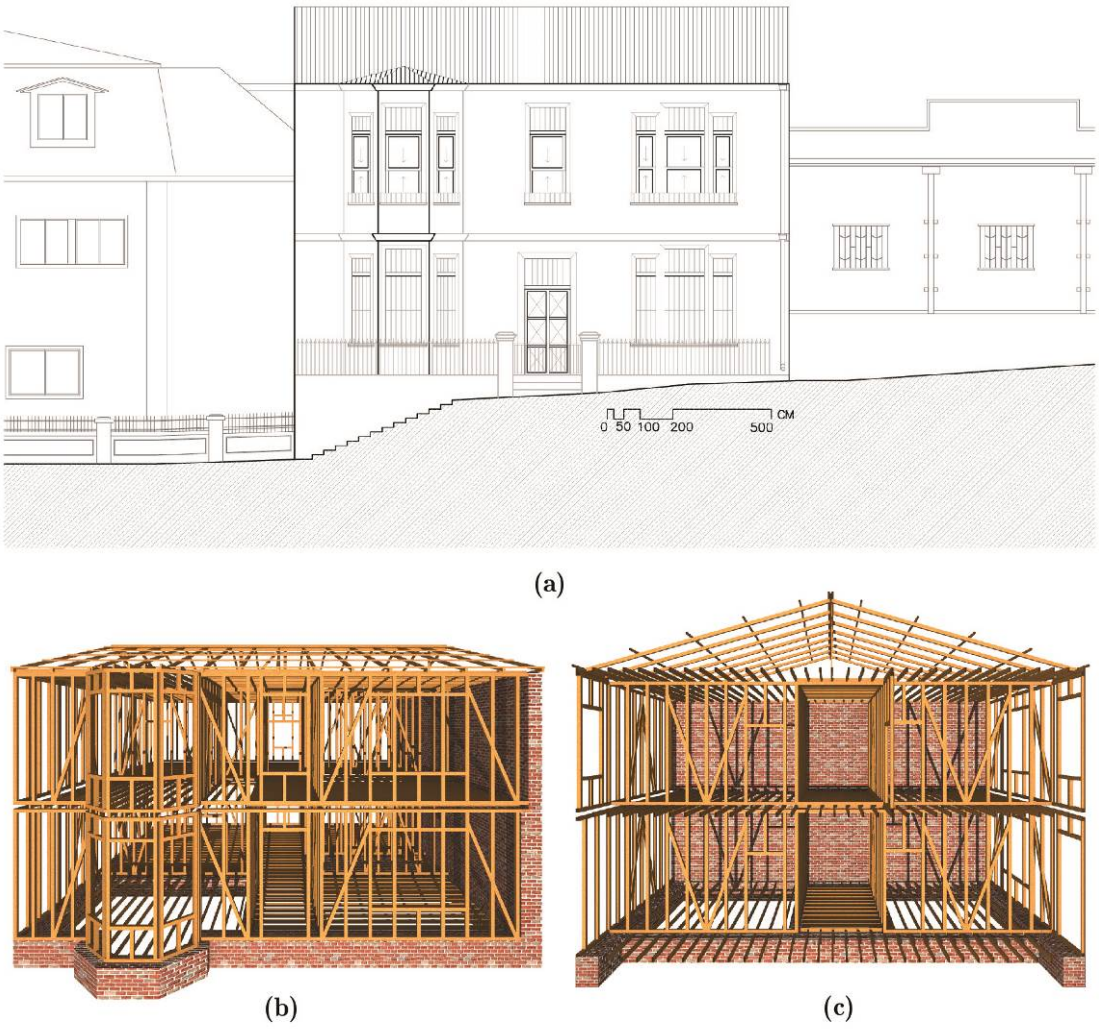

Figure 23. Drawing of the north façade of Building 2 (a) located in the number 167 of the Paseo Dimalow street in the Cerro Alegre, frontal (b) transversal (c) section views showing its structural configuration.

3.2 Numerical models of the hybrid timber-masonry structures

LPM and continuum FE models were used to simulate the nonlinear behaviour of the timber frames and masonry walls of the buildings, as shown in Figure 24a-b. Analytical calculations were executed to describe the behaviour of the carpentry joints, due to the lack of experimental data for

the specific typologies of Valparaíso. These hypotheses and assumptions were considered a reasonable approximation due to the structural similarities between the selected benchmark experiments in Section 2 and the examined cases of study. The behaviour of the timber frame structures is governed by the nonlinear behaviour of the connections, named mortise-and-tenon (stud-beam link), and connection by contact (diagonal-stud link). The rotational behaviour of mortise-and-tenon joints was investigated in previous studies (Chun, Yue, and Pan 2011; Xie et al. 2018; Chen, Qiu, and Lu 2016; Ogawa, Sasaki, and Yamasaki 2016). Analytical calculations were made in order to obtain the moment-rotation relationship of mortise-and-tenon joints, based on the simplified calculation procedure proposed by Chen, Qiu, and Lu (2016). The peak bending moment was calculated as 3.6 kNm considering the geometrical properties of the tenon, a friction coefficient of 0.25, a tangential compression strength $f_{c,t}$ = 46.65 MPa and tangential Young's modulus $E_{c,t}$ = 12798 MPa as mechanical properties of the Oak timber (Perez 1990). Nonlinear hinges were added at each mortise-and-tenon connection to model its rotational behaviour, defined with the moment-rotation relationship shown in Figure 25a.

An axial nonlinear behaviour was considered for the connections by contact, assuming the same constitutive law of the diagonal connection of the Pombalino calibrated model (see Figure 2b). The above assumption is justified by the very similar geometrical configuration and cross-section of the elements in the connections. Nonlinear axial springs acting on the horizontal translational DOF were introduced at each node where the diagonals meet the frame. Figure 25b shows the axial load-displacement relationship of the connection, with dots of different colours indicating the so-called "plastic state" of the hinges/springs within the model, according to the reached magnitude of plastic displacement/rotation. The timber material was modelled using isotropic linear elastic properties, according to the parameters of the Oak timber defined by Perez (1990).

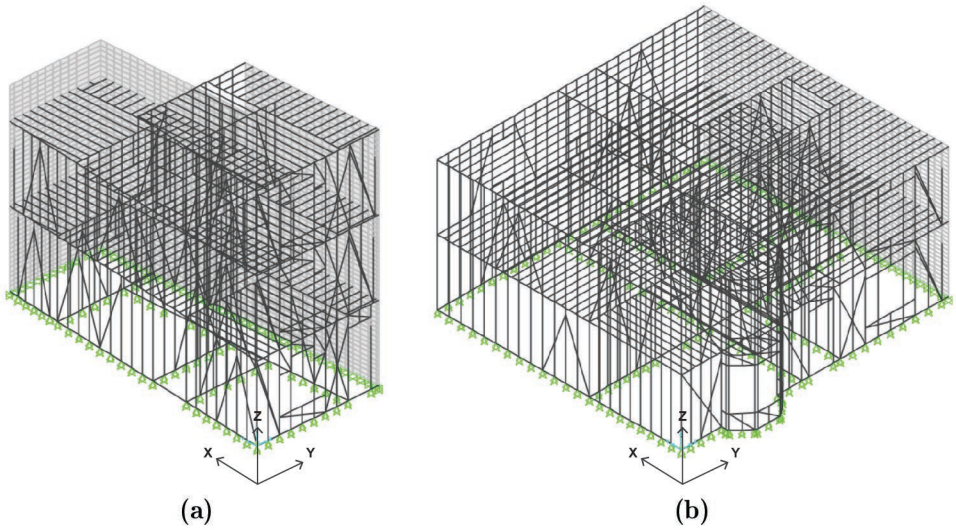

Figure 24. Numerical models of (a) Building 1 and (b) Building 2.

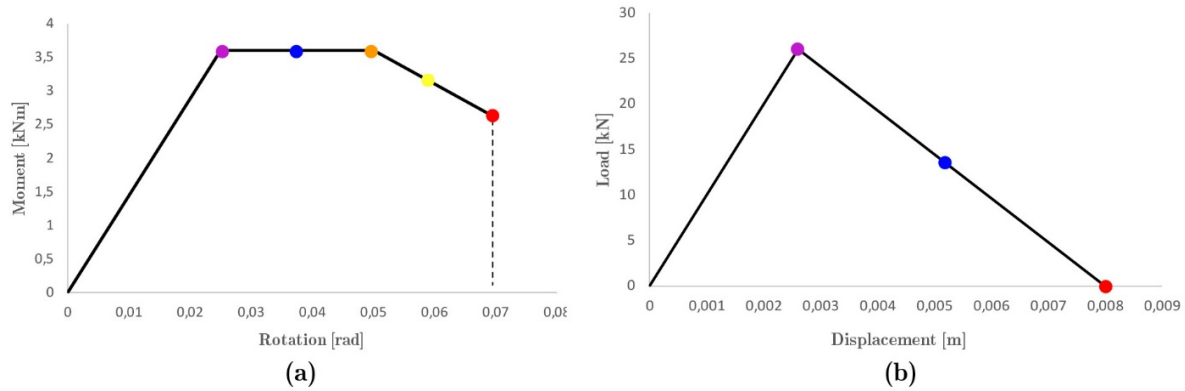

Figure 25. Constitutive laws for the carpentry joints in the lumped plasticity model of timber frames: (a) rotational behaviour of the mortise-and-tenon joints, and (b) axial behaviour of the connections by contact.

The URM walls were modelled following the continuum FE approach already described in Section 2. The uniaxial nonlinear stress-strain relationship of the material was defined considering the model proposed by Kaushik, Rai, and Jain (2007). The required mechanical properties of the material were defined based on the average characteristic values proposed by the Italian standards (Italian Ministry of Infrastructure and Transport 2018; NTC-Circolare 2018) for existing URM in solid brick and lime mortar. Reductions factor of 0.7 and 0.8 were applied respectively to compressive strength and Young's modulus values to account for thickness of mortar joints higher than 13 mm, as recommended by the Italian standards. The Young's modulus was 1.2×10^6 kN/m^2, and the

compressive strength was 2415 kN/m^2. Figure 26 displays the constitutive laws of the material both in tension and compression, assuming a tensile strength corresponding to the 5% of the compressive one. Based on the experimental studies of Kaushik, Rai, and Jain (2007) on masonry walls, the peak compressive strain capacity ε'm was considered as 0.00325 m/m, while the ultimate compressive strain was estimated as 2.75 ε'm. A friction angle of 23º was assumed to define the shear model, based on the Eurocode 6 (CEN 2005) recommendations. The fracture energy G_f of masonry was assumed as 0.05 kN/m, based on past studies on URM by Petracca et al. (2017), Lourenço (2000) and Bocca, Carpinteri, and Valente (1989). The maximum elastic strain ε_m was calculated as 1×10^{-4} m/m and the ultimate cracked strain ε_{cr} as 2.8×10^{-3} m/m. Figure 26 shows the stress-strain constitutive law, which controls the nonlinear compressive and tensile behaviour of the investigated masonry structures.

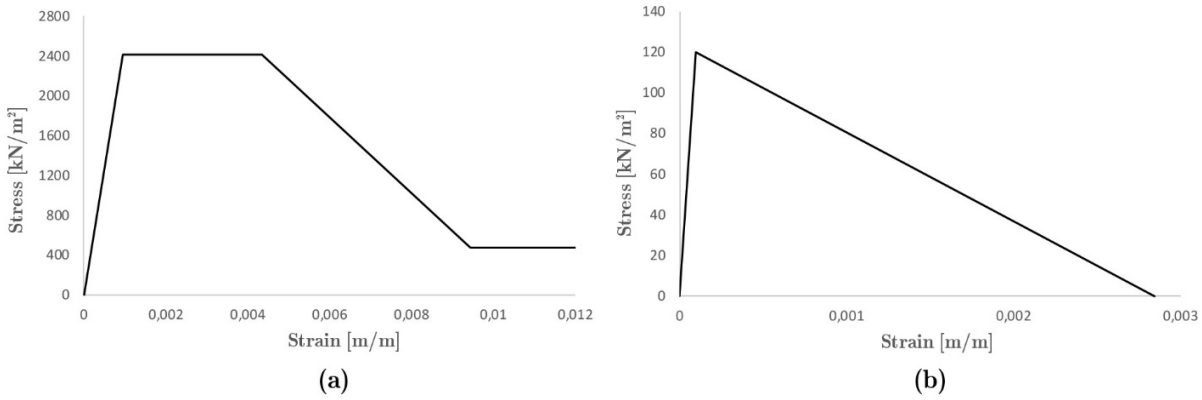

Figure 26. Uniaxial constitutive laws defining the behaviour of the masonry material for the Buildings 1 and 2: (a) compression and (b) tension stress-strain relationships.

3.3 Seismic analysis of the hybrid timber-masonry buildings

LPM of timber frames and continuum FE model of masonry walls were used to simulate the behaviour of the two cases of study. The frame elements configuring the load-bearing systems had 0.10×0.10 m^2 cross-section, except for the joists, which had 0.125×0.05 m^2 cross-section. The existence of infill in the main façade was simulated by applying the Equivalent Strut Method (ESM) considering the mechanical properties of the adobe (MINVU 2013). The internal partitions of the

buildings were modelled as bare frames since they are normally covered using other techniques such as the lath-and-plaster system.

Masonry walls were modelled using nonlinear layered shell element and two layers with four integration points each. The walls were meshed considering rectangular elements of 0.4×0.2 m^2 size. The walls of Building 1 had variable thicknesses from 0.6 m to 0.2 m from the bottom to the top levels, while the ones of Building 2 varied from 0.6 m and 0.4 m. The roofs systems were not modelled in order to simplify the analysis. This decision was made after a sensitivity analysis, which demonstrated a negligible contribution of the roof structure on the overall response of the building. Fixed and pinned supports restrained the base of masonry walls and timber frame elements respectively. These boundary conditions simulated the existence of good quality foundations.

NSA was performed along the two main directions of the models (X and Y) by applying separately horizontal forces proportional to the mass distribution of the buildings. The magnitude of the loading was increased incrementally up to the ultimate capacity of the model. The analyses were monitored in displacement control considering strategic nodes at the highest level of the structure to describe the response of the buildings. All the analyses were set using an iteration convergence tolerance of 1×10^{-4} as recommended by SAP2000 (CSI 2016).

Figure 27 displays the capacity curves obtained for the Building 1 in the X and Y directions respectively. The so-called “Model A” includes the modelling of the infill by means of the ESM, whereas “Model B” does not include the equivalent struts but maintains the inertial mass of the infill. The models A and B were examined in order to evaluate the stiffening and resisting effect of the infill. The results revealed that the building presented a higher capacity in the Y direction, as expected. The presence of equivalent struts (Model A) increased the capacity of the building analysed in the X direction in 15%, while the initial stiffness slightly incremented, as shown in Figure 27a. No significant differences were detected between the Model A and B analysed in the Y direction, as

displayed in Figure 27b. Table 4 summarizes the main results of the Model A analysed in the X and Y directions.

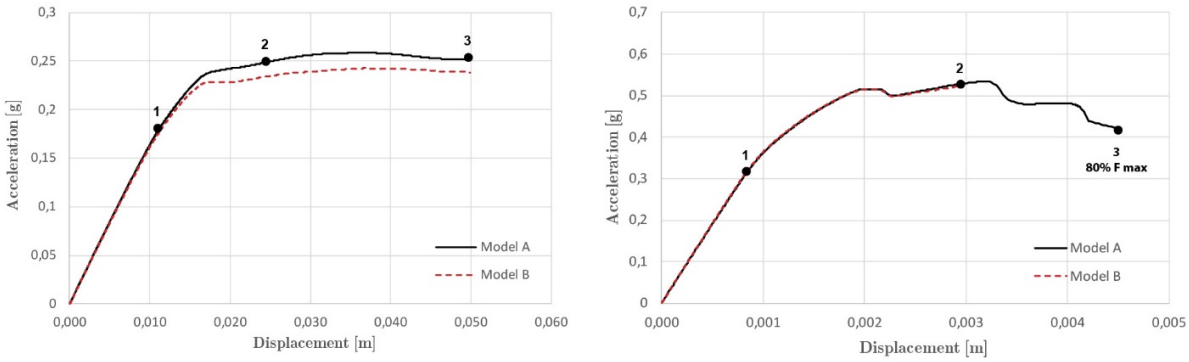

Figure 27. Capacity curves obtained for Building 1 in the (a) X and (b) Y directions.

Table 4. Summary of the results obtained for the Building 1 (Model A) in the X and Y directions.

		Maximum capacity			**Ultimate capacity**		
Building 1	Initial stiffness [kN/m]	Load [kN]	Acceleration [g]	displacement [m]	Load [kN]	Acceleration [g]	displacement [m]
X	2.58×10^4	398.5	0.26	0.037	388.7	0.25	0.050
Y	5.82×10^5	824	0.53	0.0032	653	0.42	0.0044

In the X direction, the model reached the maximum capacity at the acceleration of 0.26 g (394.2 kN base shear) and displacement of 0.034 m, whereas the ultimate displacement was recorded at 0.05 m with a slight reduction of 1.4% of shear capacity. The initial stiffness of the model was 2.58×10^4 kN/m. The building entered in the nonlinear range once a tensile crack appeared at the base of the overturning masonry wall perpendicular to the applied load (Point 1 in Figure 27a). Figure 28a displays the localization of principal tensile strains at the base the wall at the same point. The overturning mechanism around the base of the wall was activated and progressively developed (Figure 28b) until reaching the ultimate strain value of 0.0028 m/m (Figure 28b-c). The overturning mechanism of the wall also interested the connection with the perpendicular one in the final stage, with a partial formation of a vertical crack at the corner (Figure 28c). After the development of the overturning mechanism in the wall (between Points B and C in (Figure 28a), some joints plasticized

in the timber frames parallel to the applied load until reaching their ultimate capacity at the end of the analysis, as shown in Figure 28d. Most of the damaged connections were the ones located at the diagonals in tension. The overall collapse of the building is governed by the overturning of the masonry wall, which triggered the collapse of some axial springs at the diagonal elements of the frames. The redistribution of the lateral forces to the timber frame system after the failure of masonry is apparent, as shown by the capacity curve of Figure 27a.

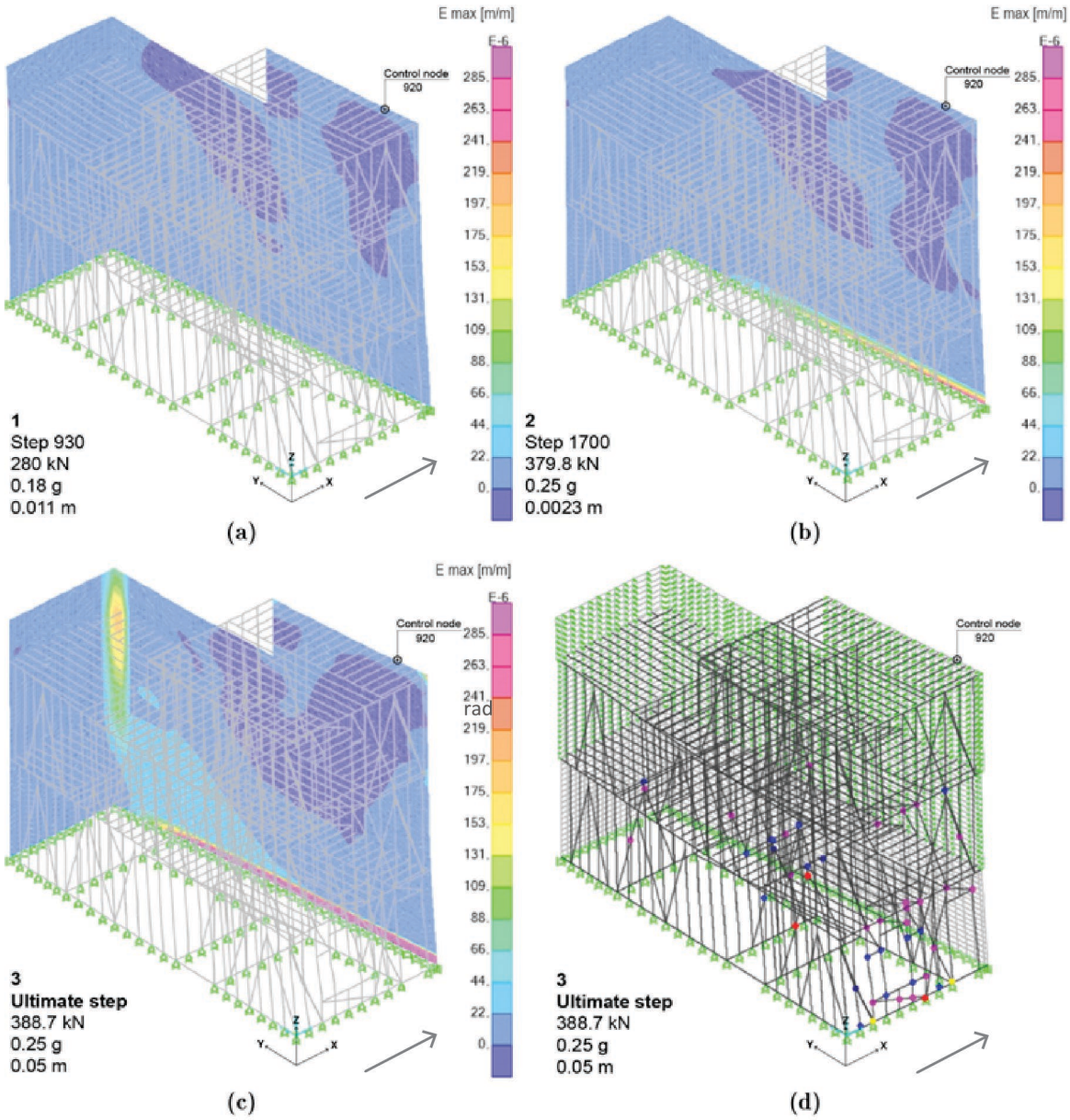

Figure 28. Seismic analysis of Building 1 in the X direction. Principal tensile strain contours (a) at a displacement of 0.011 m (Point 1 in Figure 27a), (b) at a displacement of 0.0023 m (Point 2 in Figure 27a), and at a displacement of 0.05 m (Point 3 in Figure 27a). (d) Hinges/springs plasticized at the ultimate step of the analysis in the timber frames (Point 3 in Figure 27a).

The NSA of the Building 1 in the Y direction presented almost the double of the capacity of that in the X direction, reaching 0.53 g (824 kN base shear) at a displacement of 0.0032 m. As in the X direction, the masonry walls demonstrated to play a central role in the structural response of the building. The characteristic global collapse is governed by the shear sliding at the base of the masonry wall parallel to the applied load, as shown in Figure 29. The joints of the timber frames remained elastic up to the end of the analysis, while the masonry wall parallel to the horizontal loading received the most of the seismic action due to its higher rigidity. The ultimate capacity of the building is considered as the 80% of the maximum shear base load (F_{max}), based on the Limit State definition for URM structures given by the Italian standards (NTC-Circolare 2018), being 653 kN and 0.42 g at a displacement of 0.0044 m. The initial stiffness of the model was 5.82×10^5 kN/m.

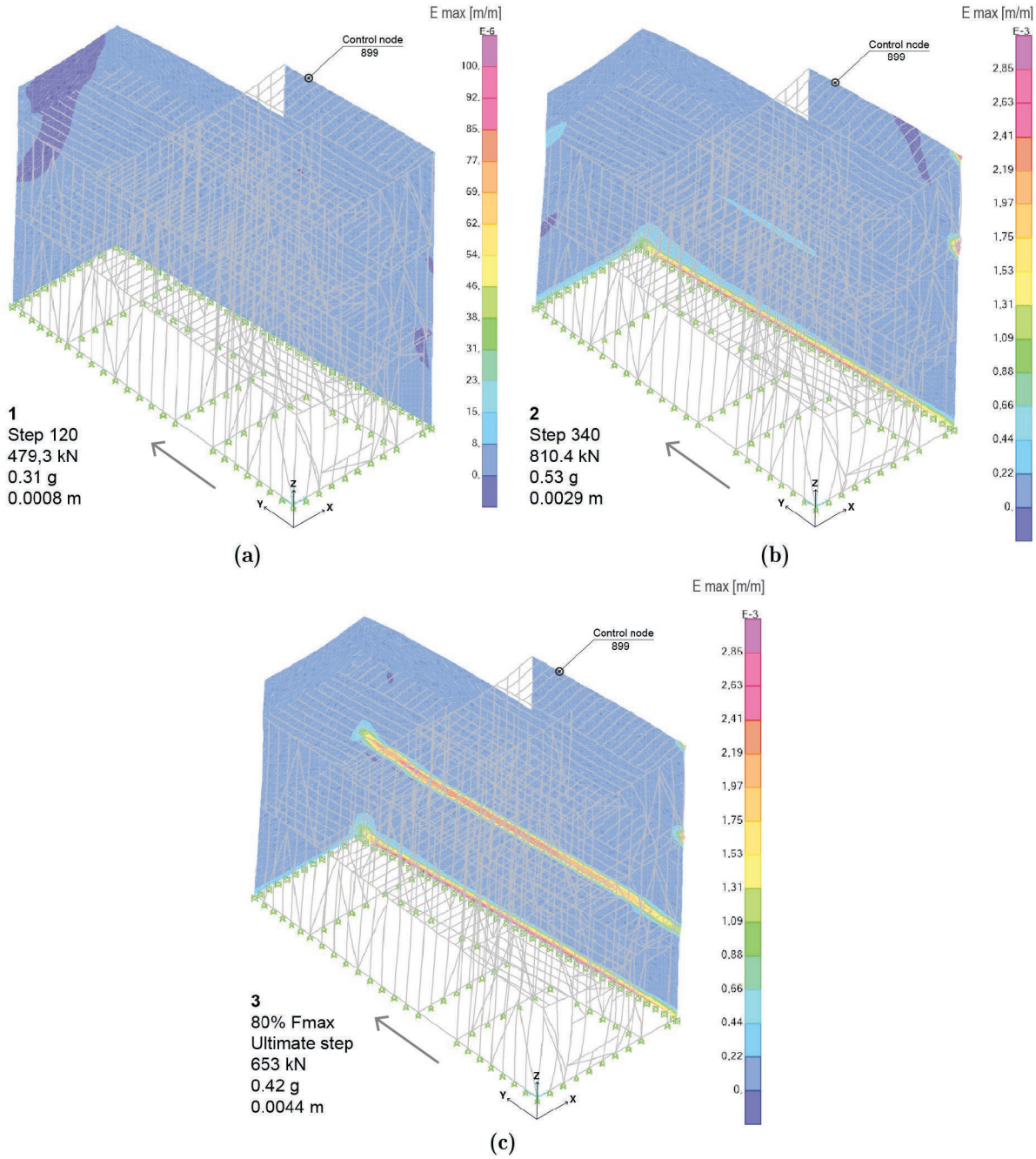

Figure 29. Seismic analysis of Building 1 in the Y direction. Principal tensile strain contours (a) at a displacement of 0.0008 m (Point 1 in Figure 27b), (b) at a displacement of 0.0029 m (Point 2 in Figure 27b), and at a displacement of 0.0044 m (Point 3 in Figure 27b).

Figure 30 displays the capacity curves obtained from the analyses of Building 2 in the X and Y directions. The results demonstrated that the building presents a higher capacity in the Y direction, as was expected. The model A presented convergence problems in the Y direction. The stiffening

effect of the equivalent struts was more evident in the Y direction analysis (Model A), as shown Figure 30b. In this case, the maximum capacity and initial stiffness of the building increased in 19% and 18%, respectively. However, there was no significant difference between Model A and B analysed in the X direction, as noted in Figure 30a. Table 5 presents a summary of the results obtained from the Model A of Building 2 for both analysis directions.

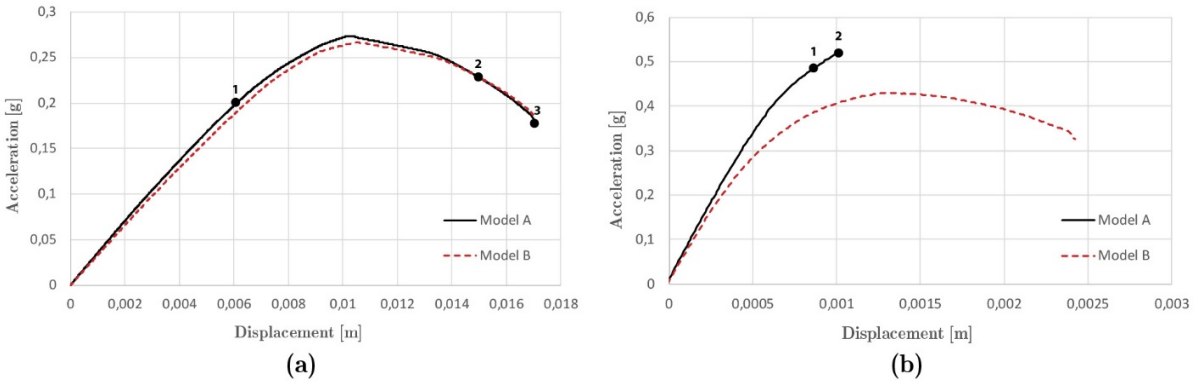

Figure 30. Capacity curves obtained for the Building 2 in the (a) X and (b) Y directions.

Table 5. Summary of the results obtained for the Building 2 simulated in the X and Y directions.

Building 2	Initial stiffness [kN/m]	Maximum capacity			Ultimate capacity		
		Load [kN]	Acceleration [g]	displacement [m]	Load [kN]	Acceleration [g]	displacement [m]
X	3.7×10^4	303.1	0.27	0.01	194.4	0.18	0.017
Y	7.4×10^5	564.8	0.52	0.001	564.8	0.52	0.001

In the X direction, the Model A reached a maximum acceleration capacity of 0.27 g (303.1 kN base shear) at a displacement of 0.0093 m, whereas the ultimate displacement was recorded at 0.017, with a significant reduction of 40% of the shear capacity. The initial stiffness of the model was 3.7×10^4 kN/m. The building entered in the nonlinear range once a horizontal crack started to appear at the base of the masonry wall as it reached the maximum tensile capacity of 0.0001 m/m. This damage is attributed to the overturning mechanism governing the failure mode of the wall. After this phase, some of the springs located in the timber frames parallel to the applied load reached their maximum capacity and plasticized progressively up to the end of the analysis. Figure 31d displayed the hinges formed at the ultimate step of the analysis. The cracking at the base of the wall

progressively developed towards the total damage at the end of the analysis, as shown in Figure 31b-c. The characteristic global collapse of the building is partially governed by the overturning mechanism of the masonry wall and the failure of some axial springs in the diagonal elements. The results reveal again a transmission of seismic forces to the timber frame elements after the failure of the wall. This response propitiates a nonlinear response of the building with a limited amount of ductility.

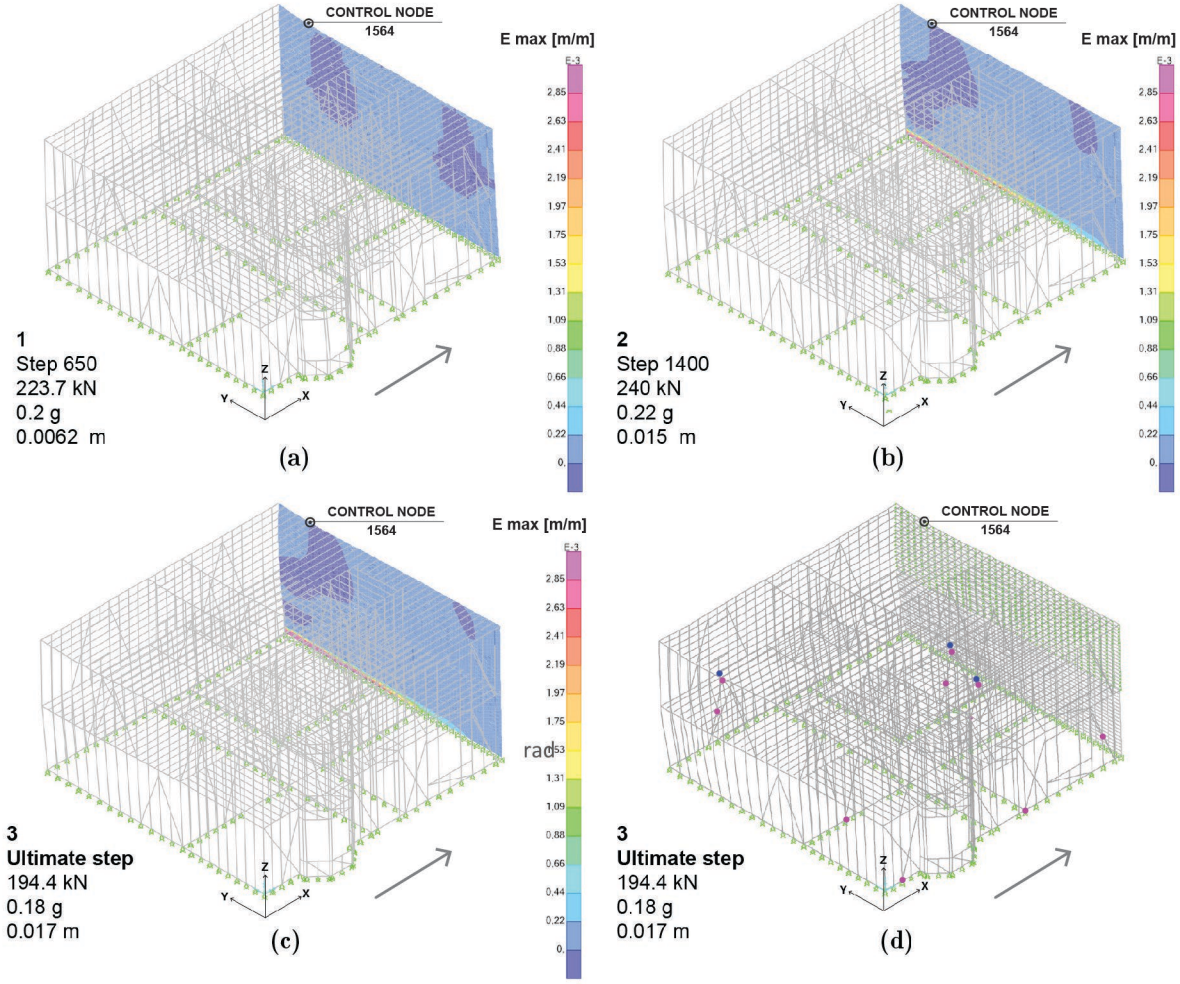

Figure 31. Seismic analysis of Building 2 in the X direction. Principal tensile strain contours (a) at a displacement of 0.0062 m (Point 1, Figure 30a), (b) at a displacement of 0.015 m (Point 2, Figure 30a), and at a displacement of 0.017 m (Point 3 in Figure 30a). (d) Hinges/springs plasticized at the ultimate step of the analysis in the timber frames (Point 3 in Figure 30a).

The NSA of Building 2 in the Y direction presented the double of the capacity of that in the X direction, reaching 0.54 g (590 kN base shear) at a displacement of 0.00011 m (Model A). The building entered in the plastic range once a horizontal cracking appeared at the base of the wall once

the maximum tensile strain of 0.0001 m/m was reached, as shown in Figure 32a. A shear sliding mechanism is activated because of the in-plane loading conditions of the wall. After this point, the cracking pattern developed a narrow damage zone until the analysis stopped due to convergence problems. The joints of the timber frames remained elastic until the end of the analysis. The convergence problems can be attributed to the quasi-brittle behaviour of the masonry, which experienced a quick drop of resistance. The analysis of the Model B, considering only the mass of the infill, reached a maximum capacity of 0.43 g (466.4 kN base shear) at a displacement of 0.0013 m, whereas the ultimate displacement was recorded at 0.0024 m with a reduction of 28% of shear capacity, as shown in Figure 32b.

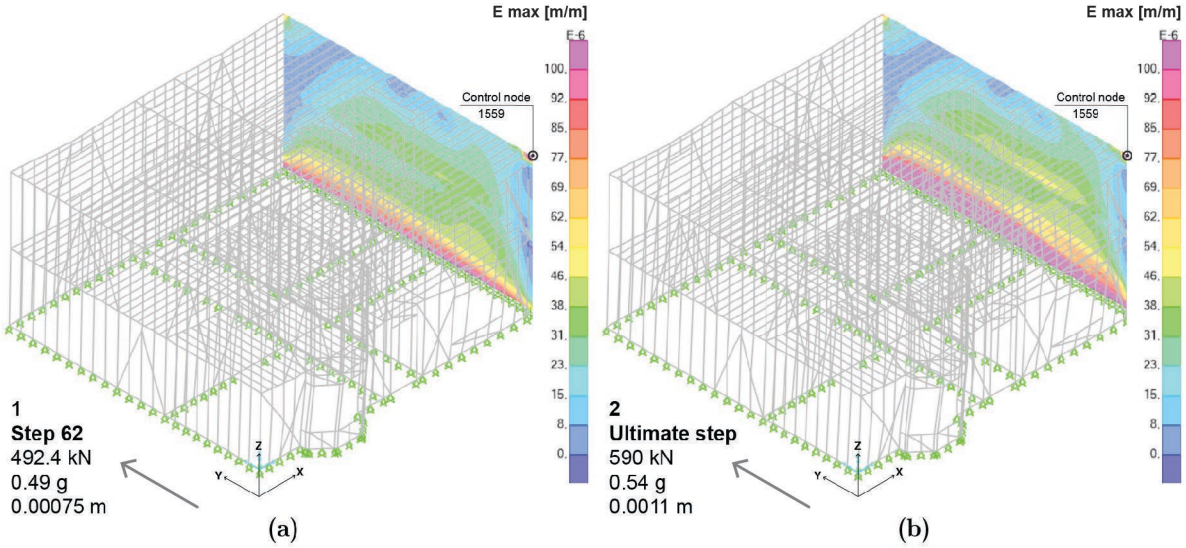

Figure 32. Seismic analysis of Building 2 in the Y direction. Principal tensile strain contours (a) at a displacement of 0.00075 m (Point 1 in Figure 30b), (b) at a displacement of 0.0011 m (Point 2 in Figure 30b).

3.4 Seismic performance of the buildings

The seismic demands of the Buildings 1 and 2 were evaluated by considering two different demand spectra. The former is calculated following the Chilean standards NCh433 Of.96 (Instituto Nacional de Normalización 2009) for a building with a soil type II and maximum ground acceleration A_0=0.4 (Zone 3). The latter corresponds to the elastic spectra of the 2010 earthquake recorded for the city of Valparaíso (Boroschek, Soto, and León 2010). Both acceleration spectra were calculated

considering a damping ratio of 0.05. Figure 33 and Figure 34 show the application of the N2 method (P. Fajfar and Eeri 2000; Peter Fajfar 1999) to Buildings 1 and 2 in the X and Y directions, respectively. Table 6 summarizes the characteristics of the equivalent SDOF systems of the two buildings for the evaluation of the seismic performance by means of the N2 method.

Table 6. Characteristics of the equivalent SDOF systems of buildings 1 and 2.

	Building 1		**Building 2**	
	X	Y	X	Y
Γ	2.03	3.94	3.57	2.67
m* [kN-s^2/m]	30.3	14.3	18.8	5.58
Fy* [kN]	188	190	80	200
dy [m]	0.0074	0.00032	0.0022	0.00026
T* [s]	0.22	0.03	0.14	0.017

The target displacement of Building 1 for the X direction-analysis is in the plastic range for the demand spectra of the Chilean seismic code, and in the elastic range, close to the yield displacement for the 2010 earthquake, see Figure 33a and Figure 33c. This means that although the 2010 earthquake did not induce notable damage to the building, for the seismic hazard foreseen by the Chilean standards the building may undergo some moderate damage. In fact, the numerical analysis in this second case shows that the masonry walls are affected by some damage, as well as some axial springs of the diagonal elements. The target displacement for the Y direction analysis remains in the elastic stage for both the demand spectra of the Chilean seismic code and the 2010 Earthquake.

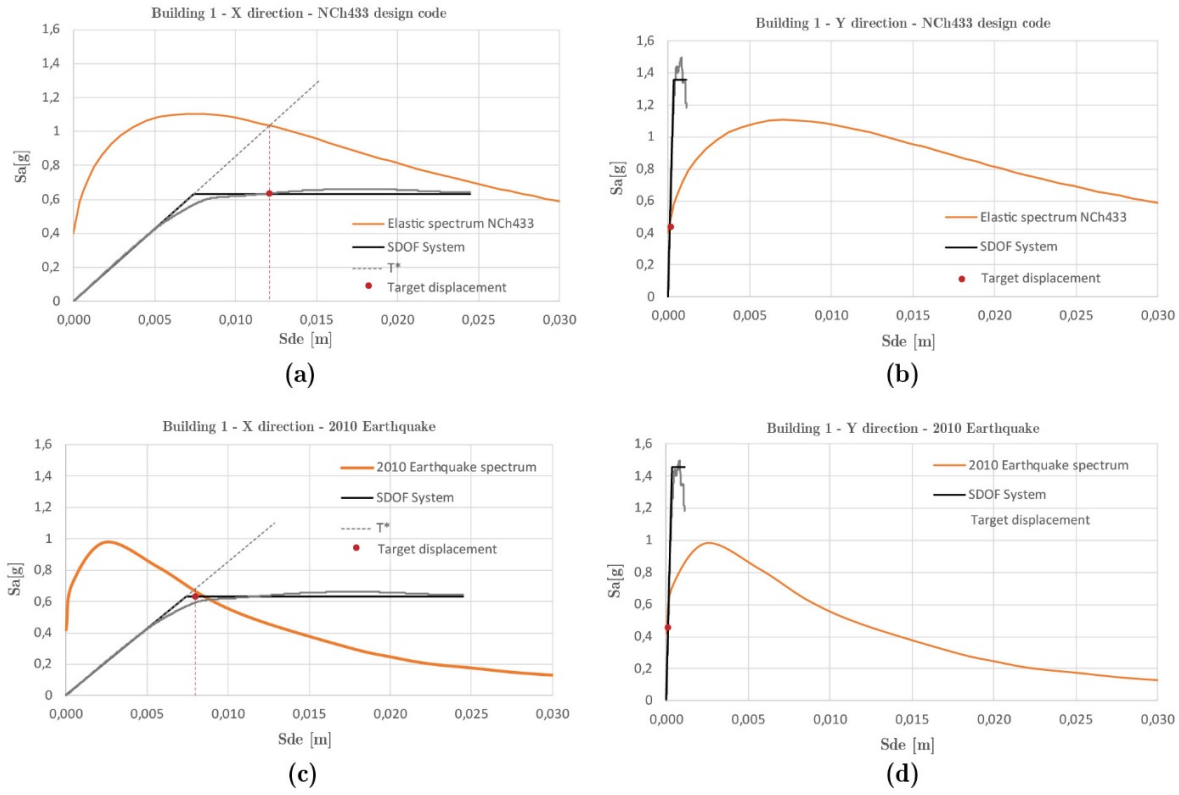

Figure 33. Application of the N2 method to Building 1 in the X and Y directions, according to the demand spectra of (a-b) the Chilean seismic code NCh433, and (c-d) of the 2010 Earthquake.

Building 2 exhibits a very good seismic performance when analysed in the Y direction, as the target displacement remains in the elastic stage for both demand spectra, as shown in Figure 34b and Figure 34d. However, the analysis in the X direction shows a target displacement rather close to the ultimate displacement for the case of the demand spectrum of the 2010 Earthquake, and target displacement higher than the ultimate one for the case of the demand spectra of the Chilean seismic code. Both results seem rather conservative if compared with the limited evidence of structural damage after the 2010 Earthquake. However, there are no data from detailed damage survey of the building after that seismic event, and the damage may have been hidden under the structure covering or by subsequent repairs. An in-situ inspection of the building executed in 2015 showed that several timber elements were recently replaced due to their bad state of conservation. In addition, it is worth noticing that the numerical analyses do not consider the actual aggregate configuration of the buildings, which would contribute to increase the structural capacity and stiffness of the system. To

conclude, it is also worth highlighting that the directionality of the earthquake is also a very important and influent parameter, as the building presents very different capacities in the X and Y direction.

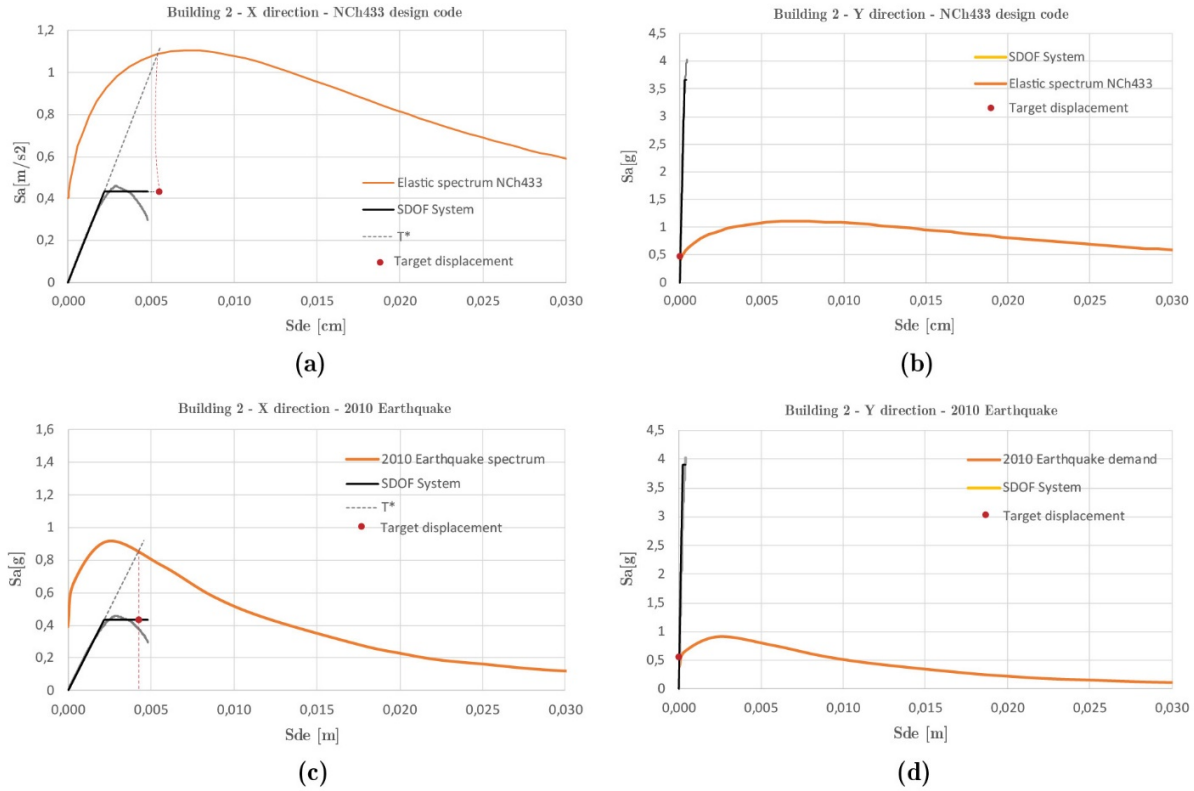

Figure 34. Application of the N2 method to Building 2 in the X and Y directions, according to the demand spectra of (a-b) the Chilean seismic code NCh433, and (c-d) of the 2010 Earthquake.

4. Conclusions

This work has presented a methodology for the seismic assessment of hybrid timber–masonry buildings based on developing simplified numerical simulations. The calibration of the numerical models has been based on the comparison with the evidence of benchmark experimental tests on timber frames and URM walls. Two timber frame typologies tested under lateral loads, i.e. the Portuguese "Pombalino" frames (Poletti 2013; Poletti and Vasconcelos 2015) and the Peruvian "*quincha"* frames (Moore and D'Ayala 2011; Torrealva, Vicente, and Michiels 2018), have been used for the calibration of the Lumped Plasticity Model (LPM). The careful stage of calibration of the LPM has considered two main parameters governing the problem, i.e., the nonlinear behaviour of the connections, and the presence of infill. The former aspect has been addressed through the

definition of nonlinear hinge and spring elements within the FE model, with proper moment-curvature or force-displacement nonlinear behaviours. The latter effect has been simulated by applying the Equivalent Strut Method (ESM). Nonlinear static analysis (NSA) has been applied to attain the results in terms of capacity curves and damage patterns. All the numerical simulations have shown satisfactory results compared with the experimental evidence. The simplified LPM of the timber frames has represented correctly the local failures of the connections occurred in the experiment, which has also allowed a good understanding of the global collapse. The contribution of the infill has been simulated by the ESM in a phenomenological and simplified manner, yet providing a good agreement with the experiments in terms of global stiffness and capacity.

Additionally, two benchmark experiments have been considered to calibrate the continuum macro-mechanical FE models of masonry, taking into account their in-plane (Augenti et al. 2011) and out-of-plane (Griffith and Vaculik 2007; Gazzola 1985) nonlinear behaviours. Masonry has been considered as a homogeneous material with average properties, defined by the constitutive model based on the theories of Darwin-Pecknold (Darwin and Pecknold 1974, 1977) and Vecchio-Collins (Frank J. Vecchio and Collins 1986). The masonry models have been capable to reproduce correctly the results of the experiments in terms of maximum capacity and collapse mechanisms, both for the in-plane and out-of-plane loaded walls. The used smeared crack model has allowed the correct identification of the overall damage mechanisms occurred in the tested walls.

The calibrated LPM and FE macro mechanical models have been adopted to analyse the seismic response of two hybrid timber-masonry buildings existent in the historical centre of Valparaíso, Chile. The LPM of the timber frame structures have been built after a proper setting of the nonlinear rotational and translational behaviours of two timber connections, i.e. the mortise-and-tenon and the connection by contact. The nonlinear constitutive law for the mortise-and-tenon has been estimated analytically based on the model proposed by Chen, Qiu, and Lu (2016), while the law of the connection by contact using the calibrated for the Pombalino frame model. The continuum

model defining the response of masonry has been defined by using the characteristic properties of existing URM and lime mortar as defined by the Italian standards (NTC-Circolare 2018).

Nonlinear Static Analysis (NSA) has been performed in the two main directions of the models (X and Y) by applying a horizontal loading pattern with forces proportional to the mass distribution of the buildings. The results have demonstrated that masonry walls have a central role in the lateral response of the buildings with hybrid timber masonry structural system, since they contribute to resist a major part of the applied loads, especially in the Y direction. In both analysis directions, the masonry walls are the first elements that reach the maximum capacity. In the Y direction, only the masonry walls reach their ultimate capacity, while the internal timber frames resist the applied actions without undergoing any damage. In this direction, the collapse of the masonry walls is given by a base shear mechanism provoked by a sliding failure at the base of the wall. In the X direction, the forces are redistributed to the timber frames after a nonlinear response of the masonry walls is triggered, and subsequently some of the springs reach their ultimate capacity. The collapse condition is given by the overturning mechanism around the base of the masonry walls, as well as the failure of the internal springs located at the diagonal connections. Both buildings have demonstrated a good seismic capacity in the Y direction.

The seismic performance of the two buildings has been assessed by applying the N2 method for two different seismic demand spectra, i.e., the earthquake design spectrum of Valparaíso bases on the NCh433 Of. 96 standards (Instituto Nacional de Normalización 2009), and the spectrum of the 2010 Earthquake occurred in the city of Valparaíso. Building 1 has confirmed its good seismic performance in the Y direction, where the target displacement has remained in the elastic range for both seismic demands. In the X direction, the target displacement has resulted slightly higher than the yield displacement for the 2010 earthquake spectrum, and in the nonlinear range for the Chilean standards demand spectrum. Almost null and moderate damage is expected respectively on the structural system for these two seismic demand levels.

Similarly, the Building 2 has presented a very good seismic performance in the Y direction for both demand spectra. In the X direction, the target displacement is very close to the ultimate displacement for the 2010 earthquake spectrum, and beyond it for the Chilean standards demand spectrum. These results would suggest important damage in both the masonry walls and timber frame connections. However, these outcomes of the numerical analyses seem rather conservative, as after the 2010 earthquake no severe damage was reported. This difference may be associated with other factors that could influence to a certain extent the seismic performance of the buildings, such as the structural aggregate condition and the actual directionality of the 2010 earthquake.

It is important to notice that the results of the research, even though based on rigorous calibration of the numerical models through careful comparisons with experimental results available in the scientific literature, are based on some tentative hypotheses that would require validation against experimental data for the buildings in Valparaíso. Due to the lack of technical documentation and test results, the research has explored the existing similarities among the buildings in Valparaíso and other similar typologies in Portugal and Peru, and has used modelling features validated for Pombalino and Quincha buildings. These assumptions have certainly introduced some simplifications that will be addressed in future research. Future studies may also evaluate in detail the effect of the aggregate condition on the buildings.

Acknowledgments

The authors gratefully acknowledge the financial support from the Ministry of Science, Innovation and Universities of the Spanish Government (MCIU), the State Agency of Research (AEI), as well as the ERDF (European Regional Development Fund), through the SEVERUS project (Multilevel evaluation of seismic vulnerability and risk mitigation of masonry buildings in resilient historical urban centres, ref. num. RTI2018-099589-B-I00). The first author gratefully acknowledges the ELARCH project (Euro-Latin America partnership in natural Risk Mitigation and protection of the Cultural Heritage, reference number 552129-EM-1-2014-1-IT- ERASMUS MUNDUS EMA21), funded by the European Commission, for the financial support of her predoctoral grant.

References

Augenti, N, F Parisi, A Prota, and G Manfredi. 2011. "In-Plane Lateral Response of a Full-Scale Masonry Subassemblage with and without an Inorganic Matrix-Grid Strengthening System." *Journal of Composites for Construction* 15 (4): 578–90. https://doi.org/10.1061/(ASCE)CC.1943-5614.0000193.

Bertodli, S. H. , Decanini, L. D., and Gavarini, C. Ottobre 1993 Telai Tamponati Soggetti ad Azione Sismiche. Un Modello Semplificato Confronto Sperimentale e Numerico 6º Convegno Nazionale L'Ingegneria Sismica in Italia Perugia 815-824

Bilgin, H., and O. Korini. 2014. "A New Modeling Approach in the Pushover Analysis of Masonry Structures." *International Students' Conference of Civil Engineering, ISCCE, May 2012, Epoka University, Tirana, Albania*.

Bocca, Pietro, Alberto Carpinteri, and Silvio Valente. 1989. "Fracture Mechanics of Brick Masonry: Size Effects and Snap-Back Analysis." *Materials and Sructures* 22: 364–73. http://staff.polito.it/alberto.carpinteri/papers/CARPINTERI_1989_N.72_MS.pdf.

Boroschek, R., P. Soto, and R. León. 2010. "Registros Del Terremoto 27 de Febrero de 2010." Santiago (Chile): Red Nacional de Acelerógrafos. Informe RENADIC.

CEN. 2005. "EN 1996-1-1: Eurocode 6: Design of Masonry Structures - Part 1-1: General Rules for Reinforced and Unreinforced Masonry Structures." https://www.phd.eng.br/wp-content/uploads/2015/02/en.1996.1.1.2005.pdf.

CEN EC5 1.2. 2004. "Eurocode 5 – Design of Timber Structures Part 1-2: General – Structural Fire Design." *Eurocode 5 – Design of Timber Structures* 2004: 1–69. https://doi.org/10.1680/cien.2001.144.6.39.

Chen, Chunchao, Hongxing Qiu, and Yong Lu. 2016. "Flexural Behaviour of Timber Dovetail Mortise-Tenon Joints." *Construction and Building Materials* 112 (June): 366–77. https://doi.org/10.1016/j.conbuildmat.2016.02.074.

Chui, Y. H., and C. Ni. 1997. "Load-Embedment Response of Timber to Reverse Cyclic Load." *Wood and Fiber Sci.* 29 (2): 148–60.

Chun, Qing, Zhi Yue, and JianWu Pan. 2011. "Experimental Study on Seismic Characteristics of Typical Mortise- Tenon Joints of Chinese Southern Traditional Timber Frame Buildings." *SCIENCE CHINA Technological Sciences* 54 (9): 2404–11. https://doi.org/10.1007/s11431-011-4448-3.

Ciocci, M. P. 2015. "Structural Analysis of the Timber Structure of Ica Cathedral, Peru. Master Thesis. Portugal: University of Minho"

Ciocci, M.P., S. Sharma, and P. B. Lourenço. 2018. “Engineering Simulations of a Super-Complex Cultural Heritage Building: Ica Cathedral in Peru.” *Meccanica* 53 (7): 1931–58. https://doi.org/10.1007/s11012-017-0720-3.

CSI. 2016. “Technical Notes Manual For SAP2000.” www.csiamerica.com.

D’Ambra, C., G.P. Lignola, and A. Prota. 2016. “Multi-Scale Analysis of In-Plane Behaviour of Tuff Masonry.” *The Open Construction and Building Technology Journal* 10 (1): 312–28. https://doi.org/10.2174/1874836801610010312.

Darwin, D, and D.A.W. Pecknold. 1974. “Inelastic Model for Cyclic Biaxial Load-Ing of Reinforced Concrete.” Urbana, Illinois: University of Illinois.

———. 1977. “Nonlinear Biaxial Stress-Strain Law for Concrete.” *Journal of the Enfineering Mechanics Division* 103 (2): 231–41.

Decanini, Luis, Fabrizio Mollaioli, Andrea Mura, and Rodolfo Saragoni. 2004. “Seismic Performance of Masonry Infilled R/C Frames.” In *13th World Conference on Earthquake Engineering.* Vancouver B. C., Canada. http://citeseerx.ist.psu.edu/viewdoc/download?doi=10.1.1.471.603&rep=rep1&type=pdf.

Endo, Yohei, Luca Pelà, Pere Roca, Francesca da Porto, and Claudio Modena. 2015. “Comparison of Seismic Analysis Methods Applied to a Historical Church Struck by 2009 L’Aquila Earthquake.” *Bulletin of Earthquake Engineering* 13 (12): 3749–78. https://doi.org/10.1007/s10518-015-9796-0.

Fajfar, P., and M. Eeri. 2000. “A Nonlinear Analysis Method for Performance Based Seismic Design.” *Earthquake Spectra*. Vol. 16.

Fajfar, Peter. 1999. “Capacity Spectrum Mehod Based on Inelastic Demand Spectra”. Earthquake Engineering & Structural Dynamics. 28(9):979-93.

Foschi, R.O. 1974. “Load-Slip Characteristics of Nails.” *Wood Science* 7 (1): 69–74.

Gazzola, E.A., Drysdale, R. G., Essawy, A. S. 1985. “Bending of Concrete Masonry Walls at Different Angles to the Bed Joints.” In *3rd North American Masonry Conference*. Arlington Texas, United States.

González, G., and J. Gutiérrez. 2005. “Structural Performance of Bamboo ‘bahareque’ Walls under Cyclic Load.” *Journal of Bamboo and Rattan* 4 (4): 353–68. https://doi.org/10.1163/156915905775008345.

Griffith, M.C, and J. Vaculik. 2007. “Out-of-Plane Flexural Strength of Unreinforced Clay Brick Masonry Walls.” *TMS Journal*, 25 (1): 53–68.

Hordijk, D.A. 1991. “Local Approach to Fatigue of Concrete”. Doctoral Thesis. Delf, Netherlands:

Delft University of Technology. https://repository.tudelft.nl/islandora/object/uuid%3Afa87147b-8201-47ed-83d7-b812b09c5fbb.

Instituto Nacional de Normalización. 2009. “NCh433.Of1996 Modificada En 2009 - Earthquake Resistant Design of Buildings,” 1–43. http://ecommerce.inn.cl/index.php.

Italian Ministry of Infrastructure and Transport. 2018. “NTC 2018 - D.M. 17.01.18: Aggiornamento Delle ‘Norme Tecniche per Le Costruzioni,’” 1–198.

Jiménez, B. 2015. “Los Entramados Tradicionales de Madera En Los Cerros Alegre y Concepción. Caracterización Histórica y Técnica de Las Viviendas de Finales Del Siglo XIX y Comienzos Del XX.” Tesis de grado. Valparaíso, Chile: Universidad Técnica Federico Santa María.

———. 2021. “Seismic Vulnerability Assessment of Traditional Timber Frame and Masonry Wall Buildings : Aplication to the Historical Centre of Valparaíso, Chile.” *TDX (Tesis Doctorals En Xarxa)*. Barcelona, Spain: Universitat Politècnica de Catalunya. http://www.tdx.cat/handle/10803/671491.

Jiménez, B., Luca Pelà, and M Hurtado. 2018. “Building Survey Forms for Heterogeneous Urban Areas in Seismically Hazardous Zones. Application to the Historical Center of Valparaíso, Chile.” *International Journal of Architectural Heritage* in press.

Jiménez, Belén, Savvas Saloustros, and Luca Pelà. 2021. “Seismic Vulnerability Index Method for Hybrid Timber–Masonry Structures. Numerical Calibration and Application to the City of Valparaíso, Chile.” *Journal of Building Engineering* 44 (December): 103185. https://doi.org/10.1016/J.JOBE.2021.103185.

Kalkbrenner, P., L. Pelà, and C. Sandoval. 2019. “Multi Directional Pushover Analysis of Irregular Masonry Buildings without Box Behavior.” *Engineering Structures* 201 (December): 109534. https://doi.org/10.1016/j.engstruct.2019.109534.

Kaushik, Hemant B., Durgesh C. Rai, and Sudhir K. Jain. 2007. “Stress-Strain Characteristics of Clay Brick Masonry under Uniaxial Compression.” *Journal of Materials in Civil Engineering* 19 (9): 728–39. https://doi.org/10.1061/(ASCE)0899-1561(2007)19:9(728).

Kouris, L..A.S, Meireles, A.J. Kappos, and R Bento. 2014. “Simple and Complex Modelling of Timber-Framed Masonry Walls in Pombalino Buildings.” Bulletin of Earthquake Engineering. 12 (4): 1777-803. https://doi.org/10.1007/s10518-014-9586-0.

Kouris, L.A.S., and A.J. Kappos. 2012. “Detailed and Simplified Non-Linear Models for Timber-Framed Masonry Structures.” *Journal of Cultural Heritage* 13 (1): 47–58. https://doi.org/10.1016/j.culher.2011.05.009.

———. 2014. “A Practice-Oriented Model for Pushover Analysis of a Class of Timber-Framed Masonry Buildings.” *Engineering Structures* 75: 489–506. https://doi.org/10.1016/j.engstruct.2014.06.012.

Lourenço, Paulo B. 2000. “Anisotropic Softening Model for Masonry Plates and Shells.” *Journal of Structural Engineering* 126 (9): 1008–16. https://doi.org/10.1061/(ASCE)0733-9445(2000)126:9(1008).

Lukic, R., E. Poletti, H. Rodrigues, and G. Vasconcelos. 2018. “Numerical Modelling of the Cyclic Behavior of Timber-Framed Structures.” *Engineering Structures* 165 (March): 210–21. https://doi.org/10.1016/j.engstruct.2018.03.039.

MINVU. 2013. “NTM 002 Proyecto de Intervención Estructural de Construcciones de Tierra NTM 022.”ISBN 978-956-7674-92-3.

Moore, D, and D. D’Ayala. 2011. “Racking Behaviour of Traditional Peruvian Shear Walls.” MEng Civil Engineering Undergraduate Dissertation. Bath: University of Bath.

NTC-Circolare. 2018. “Circolare 21 Gennaio 2019 n. 7 C.S.LL.PP. Istruzioni per l’applicazione Dell’aggiornamento Delle ‘Norme Tecniche per Le Costruzioni’ Di Cui Al D.M. 17/01/2018.” *Consiglio Superiore Dei Lavori Pubblici*.

Ogawa, Keita, Yasutoshi Sasaki, and Mariko Yamasaki. 2016. “Theoretical Estimation of the Mechanical Performance of Traditional Mortise–Tenon Joint Involving a Gap.” *Journal of Wood Science* 62 (3): 242–50. https://doi.org/10.1007/s10086-016-1544-9.

Pantò, B., L. Silva, G. Vasconcelos, and P. B. Lourenço. 2019. “Macro-Modelling Approach for Assessment of out-of-Plane Behavior of Brick Masonry Infill Walls.” *Engineering Structures* 181 (August 2018): 529–49. https://doi.org/10.1016/j.engstruct.2018.12.019.

Perez Galaz, V. 1990. “Manual de Cálculo de Construcciones En Madera 2a.” Santiago (Chile): INFOR.

Perrone, M. 2011. “Study of El Comercio Hotel, Lima (Peru). Numerical Modelling of a Historic Earthen Building Made of Non-Conventional Materials and Located in Seismic Zones". Doctoral Thesis. Chieti-Pescara: Universita’ degli Studi “G. d’Annunzio” Chieti-Pescara.

Petracca, Massimo, Luca Pelà, Riccardo Rossi, Sergio Oller, Guido Camata, and Enrico Spacone. 2017. “Multiscale Computational First Order Homogenization of Thick Shells for the Analysis of Out-of-Plane Loaded Masonry Walls.” *Computer Methods in Applied Mechanics and Engineering* 315: 273–301. https://doi.org/10.1016/j.cma.2016.10.046.

Poletti, E. 2013. “Characterization of the Seismic Behaviour of Traditional Timber Frame Walls”. Doctoral Thesis. Minho, Portugal: Universidade do Minho.

Poletti, E., P.B. Lourenco, and M. P. Ciocci. 2016. “Numerical Approaches for the Analysis of Timber Frame Walls Numerical Analysis.” In *Historical Earthquake-Resistant Timber Framing in the Mediterranean Area. HEaRT 2015.*, edited by Helena Cruz and et al., 183–92. Springer Nature. https://doi.org/10.1007/978-3-319-39492-3.

Poletti, E., and G. Vasconcelos. 2015. “Seismic Performance of Traditional Half-Timbered Walls: Experimental Results.” In *Historical Earthquake-Resistant Timber Frames in the Mediterranean Area*, edited by Nicola Ruggieri, Gennaro Tampone, and Raffaele Zinno, 171. Switzerland: Springer, Cham.

Porteous, J., and A. Kermani. 2004. *Structural Timber Design to Eurocode 5*. 2nd ed. Vol. 2004. Oxford: Blackwell Science Ltd. https://doi.org/10.1680/cien.2001.144.6.39.

Quinn, N. 2016. “Structural Characterization and Numerical Modeling of Historic Quincha Walls Structural Characterization and Numerical Modeling of Historic Quincha Walls.” *International Journal of Architectural Heritage*. https://doi.org/10.1080/15583058.2015.1113337.

Reinhardt, Hans Walter. 1984. “Fracture Mechanics of an Elastic Softening Material like Concrete.” https://www.semanticscholar.org/paper/Fracture-Mechanics-of-an-Elastic-Softening-Material-Reinhardt/78a8ccfe2f84bf4bc0646d5dde0fd2c7182d11fe.

Roca, Pere, Miguel Cervera, Giuseppe Gariup, and Luca Pela’. 2010. “Structural Analysis of Masonry Historical Constructions. Classical and Advanced Approaches.” *Archives of Computational Methods in Engineering* 17 (3): 299–325. https://doi.org/10.1007/s11831-010-9046-1.

Saloustros, S., L. Pelà, and P. Roca. 2020. “Nonlinear Numerical Modeling of Complex Masonry Heritage Structures Considering History-Related Phenomena in Staged Construction Analysis and Material Uncertainty in Seismic Assessment.” *Journal of Performance of Constructed Facilities* 34 (5): 04020096. https://doi.org/10.1061/(asce)cf.1943-5509.0001494.

Saloustros, Savvas, Miguel Cervera, and Luca Pelà. 2019. “Challenges, Tools and Applications of Tracking Algorithms in the Numerical Modelling of Cracks in Concrete and Masonry Structures.” *Archives of Computational Methods in Engineering* 26 (4): 961–1005. https://doi.org/10.1007/s11831-018-9274-3.

Saloustros, Savvas, Luca Pelà, Miguel Cervera, and Pere Roca. 2017a. “Finite Element Modelling of Internal and Multiple Localized Cracks.” *Computational Mechanics* 59 (2): 299–316. https://doi.org/10.1007/s00466-016-1351-6.

———. 2017b. “An Enhanced Finite Element Macro-Model for the Realistic Simulation of Localized Cracks in Masonry Structures: A Large-Scale Application.” International Journal of

Architectural Heritage. 12 (3): 432-47. https://doi.org/10.1080/15583058.2017.1323245.

Sassun, Kathy, Timothy J Sullivan, Paolo Morandi, and Donatello Cardone. 2016. “Characterising the In-Plane Seismic Performance of Infill Masonry.” *Bulletin of the New Zealand Society for Earthquake Engineering* Vol 49 (No. 1): 100–117.

Spyrakos, C., and A Francioso. 2012. “Shaking Table Test and Pushover Analysis on a Scaled Masonry Building.” *15th World Conference on Earthquake Engineering*. Lisbon: Sociedade Portuguesa de Engenharia Sísmica.

Stafford-Smith, B. 1963. “Lateral Stiffness of Infilled Frames.” *Journal of Structural Division, ASCE* Vol.88 (No. ST 6): pp 183-199.

Torrealva, D., E. Vicente, and T. Michiels. 2018. “Testing of Materials and Building Components of Historic Adobe Buildings in Peru”. Los Angeles: Getty Conservation Institute. https://hdl.handle.net/10020/gci_pubs/testing_materials.

Turnšek, V, and P Sheppard. 1980. “The Shear and Flexural Resistance of Masonry Walls.” In *International Research Conference on Earthquake Engineering.* IEEES (Skopje), 517–73.

Vecchio, F. J., and M. P. Collins. 1993. “Compression Response of Cracked Reinforced Concrete.” *Journal of Structural Engineering* 119 (12): 3590–3610. https://doi.org/10.1061/(ASCE)0733-9445(1993)119:12(3590).

Vecchio, Frank J., and Michael P. Collins. 1986. “The Modified Compression-Field Theory for Reinforced Concrete Elements Subjected to Shear.” *ACI Journal Proceedings* 83 (2): 219–31. https://doi.org/10.14359/10416.

Vieux-champagne, F., G. Stéphane, Y. Sieffert, P. Garcia, C. Faye, J. C. Duccini, and L. Daudeville. 2014. “Numerical Analysis of Timber-Frame Structures with Infill under Seismic Loading". World Conference on Timber Engineering (WCTE 2014). Quebec, Canada. 1912-1919.

Xie, Qifang, Long Wang, Peijun Zheng, Lipeng Zhang, and Weibing Hu. 2018. “Rotational Behavior of Degraded Traditional Mortise-Tenon Joints : Experimental Tests and Hysteretic Model.” *International Journal of Architectural Heritage* 12 (1): 125–36. https://doi.org/10.1080/15583058.2017.1390629.

Xu, Jian. 2006. “Development of a General Dynamic Hysteretic Light-Frame Structure Model and Study on the Torsional Behavior of Openfront Light-Frame Structures”. Doctoral Thesis. Whashington: Department of Civil & Environmental Engineering, Washington State University.